

# 3

1979

1980

## Physics of Resistive plate chambers

1981 The Resistive Plate Chamber (RPC) has been developed in 1981 by Santonico and Cardarelli [178],  
1982 under the name of *Resistive Plate Counter*, as an alternative to the local-discharge spark counters  
1983 proposed in 1978 by Pestov and Fedotovich [179, 180]. Working with spark chambers implied using  
1984 high-pressure gas and high mechanical precision which the RPC simplified by formerly using a gas  
1985 mixture of argon and butane at atmospheric pressure and a constant and uniform electric field gener-  
1986 ated in between two parallel electrode plates. Moreover, a significant increase in rate capability was  
1987 introduced by the use of electrode plate material with high bulk resistivity, preventing the discharge  
1988 from growing throughout the whole gas gap. Indeed, the effect of using resistive electrodes is that  
1989 the constant electric field is locally canceled out by the development of the discharge, limiting its  
1990 growth.

1991 Through its development history, different operating modes [181–183], gas mixtures [178, 183–  
1992 188] and new detector designs [189–191] have been discovered, leading to further improvement  
1993 of the rate capability of such a detector. The low construction costs and easily achievable large  
1994 detection areas offered by RPCs, as well as the wide range of possible designs, made them a natural  
1995 choice as muon chambers and/or trigger detectors in multipurpose experiments such as CMS [192]  
1996 or ATLAS [193], time-of-flight detectors in ALICE [194], calorimeters with CALICE [195] or even  
1997 detectors for volcanic muography with ToMuVol [196].

1998 In this chapter, the general operating principles of RPCs will be introduced leading to a deeper  
1999 description of the parameters having an influence on the rate capability and the time resolution such  
2000 detectors. Even though the principle behind the operation of RPCs might seem straight forward,  
2001 attempts at proposing a model of the signal formation inside of the gas volume have so far failed at  
2002 fully explain what can be observed from the data. A detailed summary of the understanding of RPC  
2003 physics will be provided. Finally, more practical information will be given on the influence of the  
2004 environment on the operation of a real detector. The changing conditions might alter the collected  
2005 data and needs to be addressed in order to limit the systematics on the final results.

2006 **3.1 Principle**

2007 RPCs are proportional counters composed of two parallel resistive plate electrodes in between which  
2008 a constant electric field is set. The space in between the electrodes, referred to as *gap*, is filled with  
2009 a gas that is used to generate primary ionization into the gas volume. The free charge carriers (elec-  
2010 trons and cations) created by the ionization of the gas molecules are then accelerated towards the  
2011 electrodes by the electric field, as shown in Figure 3.1 [197]. Since RPCs are passive detectors, a  
2012 current on copper pick-up strips or pads placed outside of the gas volume is induced by the charge  
2013 accumulation during the growth of the avalanche resulting from the acceleration of the charge car-  
2014 riers. As a consequence, the time resolution of the detector is substantially increased compared to  
2015 detectors using charge collection at the level of the electrode as the output signal is generated by  
2016 the movement of the electrons in the electric field. The advantage of a constant electric field, over  
2017 multi-wire proportional chambers, is that the electrons are being fully accelerated from the moment  
2018 charge carriers are freed. They feel the full strength of the electric field that doesn't depend on the  
2019 distance to the readout.

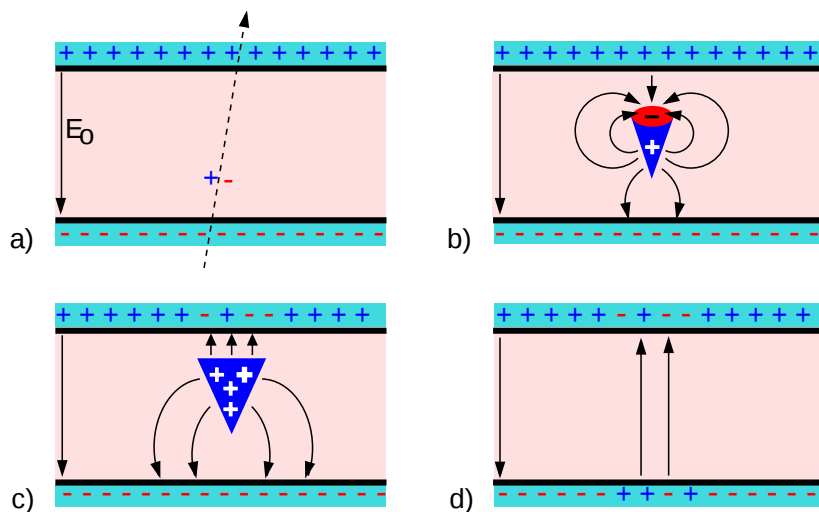


*Figure 3.1: Different phases of the avalanche development in the RPC gas volume subjected to a constant electric field  $E_0$ . a) An avalanche is initiated by the primary ionisation caused by the passage of a charged particle through the gas volume. b) Due to its growing size, the avalanche starts to locally influence the electric field. c) The electrons, lighter than the cations reach the anode first. d) The ions reach the cathode. While the charges have not recombined, the electric field in the small region around the avalanche stays affected and locally blinds the detector.*

2020 After an avalanche developed in the gas, a time long compared to the development of a discharge  
2021 is needed to recombine the charge carriers in the electrode material due to its resistivity. This prop-  
2022 erty has the advantage of affecting the local electric field only, and avoiding sparks in the detector  
2023 but, on the other hand, the rate capability is intrinsically limited by the time constant  $\tau_{RPC}$  of the  
2024 detector. Using a quasi-static approximation of Maxwell's equations for weakly conducting media,  
2025 it can be shown that the time constant  $\tau_{RPC}$  related to the charge recombination at the interface in

2026 between the electrode and the gas volume is given by Equation 3.1 [198].

$$(3.1) \quad \tau_{RPC} = \frac{\epsilon_{electrode} + \epsilon_{gas}}{\sigma_{electrode} + \sigma_{gas}}$$

2027 A gas can be assimilated to vacuum, leading to  $\epsilon_{gas} = \epsilon_0$  and  $\sigma_{gas} = 0$ , and the electrodes  
 2028 permittivity and conductivity can be written as  $\epsilon_{electrode} = \epsilon_r \epsilon_0$  and  $\sigma_{electrode} = 1/\rho_{electrode}$ ,  
 2029 showing the strong dependence of the time constant on the electrodes resistivity in Formula 3.2.

$$(3.2) \quad \tau_{RPC} = (\epsilon_r + 1)\epsilon_0 \times \rho_{electrode}$$

2030 The resistivity targeted to build RPCs ranges from  $10^9$  to  $10^{12} \Omega \cdot \text{cm}$ . Very few materials with  
 2031 a low enough resistivity exist in nature. The most common RPC electrode materials are displayed in  
 2032 Table 3.1. When the doped glass and ceramics can offer short time constants of the order of 1 ms,  
 2033 the developing cost of such materials is quite high due to the very low demand. Thus, High-Pressure  
 2034 Laminate (HPL) is often the choice for high-rate experiments using very large RPC detection areas.  
 2035 To be effectively used, the surface of HPL electrodes requires a linseed oil treatment which allows  
 2036 for a lower intrinsic noise rate and dark current of the detectors by improving the smoothness of the  
 2037 electrodes surface [199]. Other experiments working at cosmic muon fluxes can safely operate with  
 2038 ordinary float glass.

Material	$\rho_{electrode} (\Omega \cdot \text{cm})$	$\epsilon_r$	$\tau_{RPC}$ (ms)
Float glass	$10^{12}$	~7	~700
High-Pressure Laminate	$10^{10}$ to $10^{12}$	~6	~6 to 600
Doped glass (LR S)	$10^9$ to $10^{11}$	~10	~1 to 100
Doped ceramics (SiN/SiC)	$10^9$	~8.5	~1
Doped ceramics (Ferrite)	$10^8$ to $10^{12}$	~20	~0.2 to 2000

Table 3.1: Properties of the most used electrode materials for RPCs.

## 2039 3.2 Rate capability and time resolution of Resistive Plate Chambers

2041 The electrode material plays a key role in the maximum intrinsic rate capability of RPCs. R&D is  
 2042 continuously being done to develop at always cheaper costs material with lower resistivity. Never-  
 2043 theless, the amount of charge released, i.e. the size of the discharge, if reduced leads to a smaller  
 2044 blind area in the detector, increasing the rate capability of the detector. On the other hand, the drift  
 2045 velocity of electrons in the gas volume being quite stable with the applied electric field, the design of  
 2046 a detector and the associated read-out and pulse-processing electronics will be a major component  
 2047 of the time resolution of RPCs. Moreover, the sensitivity of the electronics will also help increasing  
 2048 the rate capability. An improved sensitivity will allow for a lower gain to operate the detector. This  
 2049 will result in a more spatially contained signal development.

### 2050 3.2.1 Operation modes

2051 Being a gaseous detector using an accelerating electric field to amplify the signal of primary charge  
 2052 carriers, the RPC can be operated in different modes depending on the electric field intensity. Each

mode offers different performances for such a detector, and it will be showed that the operating mode corresponding to the lowest electric field possible is best suited for high-rate detectors working in collider experiments.

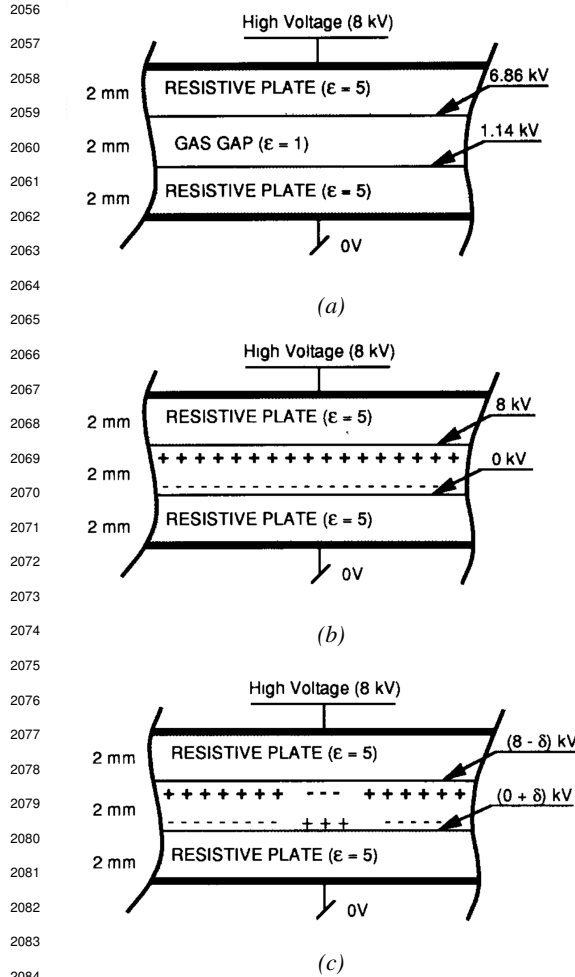


Figure 3.2: Movement of the charge carriers in an RPC. (a): Voltage across an RPC whose electrodes have a relative permittivity of 5 at the moment the tension is applied. (b): After the charge carriers moved, the electrodes are charged and there is no voltage drop over the electrodes anymore. The full potential is applied over the gas gap only. (c): The streamer discharge initiated by a charged particle transports electrons and cations towards the anode and cathode respectively.

ode and the positive ion cloud remains much smaller. The positive ion cloud remains much smaller. The resulting signal is weaker, of the order of a few mV as shown on Figure 3.3, and requires amplification. This is the *avalanche mode* of RPC operation. This mode offers a higher rate capability by providing smaller discharges that don't affect the electrodes charge and are more locally contained in the gas volume as was demonstrated by Crotty with Figure 3.4 [181]. The detector only stays locally blind the time the charge carriers

RPCs were developed early 1980s. At that time they were used in an operating mode now referred to as *streamer mode*. Streamers are large discharges that develop in between the two electrodes far enough to locally discharge the electrodes. If the electric field inside of the gas volume is strong enough, a large and dense cloud of positive ions will develop near the anode and extend toward the cathode. Indeed, the electrons traveling faster will be collected leaving the gas region near the anode filled with positively charged ions. The field is then strong enough so that electrons are pulled out of the cathode leading to a streamer discharge. Electrodes, though they are a unique volume of resistive material, can be assimilated to capacitors. At the moment an electric field is applied between their outer surfaces, the charge carriers inside of the volume will start moving leading to a situation where there is no potential difference across the electrodes and a higher density of negative charges, i.e. electrons, on the inner surface of the cathode. Finally, when a streamer discharge occurs, these electrons are partially released in the gas volume contributing to increase the discharge strength until the formation of a conductive plasma, the streamer. This can be understood through Figure 3.2 [181]. Streamer signals are very convenient in terms of read-out as no further amplification is required with output pulses amplitudes of the order of a few tens to few hundreds of mV as can be seen on Figure 3.3.

In contrast to the above, when the electric field is lowered, the electronic gain is reduced until the electrons get close enough to the anode. The electric field doesn't reach the point where a field emission of electrons on the cathode is possible. The resulting signal is weaker, of the order of a few mV as shown on Figure 3.3, and requires amplification. This is the *avalanche mode* of RPC operation. This mode offers a higher rate capability by providing smaller discharges that don't affect the electrodes charge and are more locally contained in the gas volume as was demonstrated by Crotty with Figure 3.4 [181]. The detector only stays locally blind the time the charge carriers

2099 are recombined and there is no need for electrode recharge which is a long process affecting a large  
 2100 portion of the detector. Another advantage of avalanche signals over streamers is the better time  
 2101 consistency. Figure 3.3 shows very clearly that avalanche signals have a very small time jitter. Using  
 2102 such a mode is a natural choice for experiments in which the detectors are required to have a high  
 2103 detection rate.

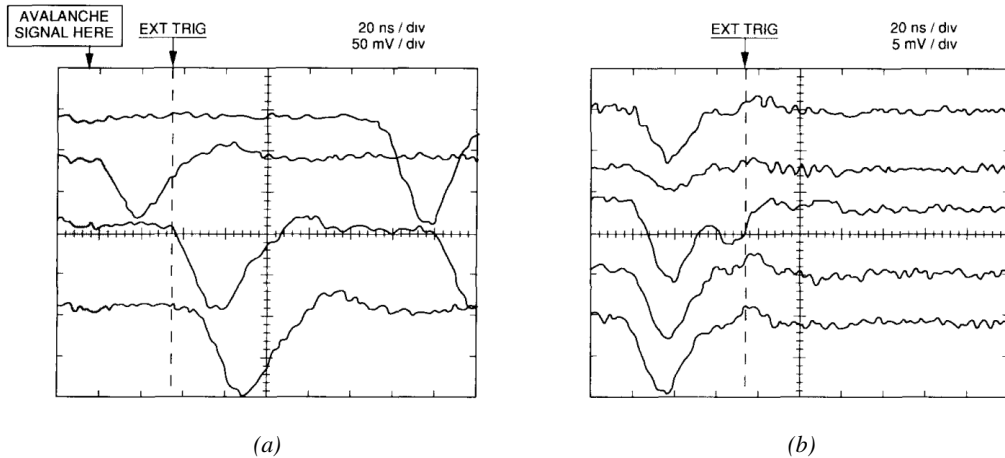


Figure 3.3: Typical oscilloscope pulses in streamer mode (a) and avalanche mode (b). In the case of streamer mode, the very small avalanche signal is visible.

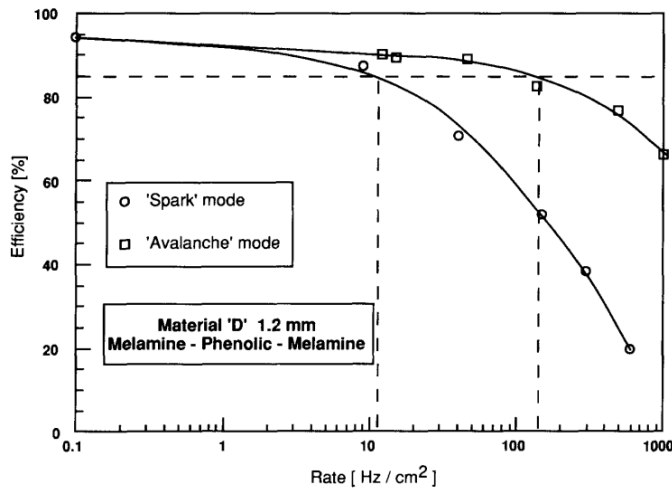
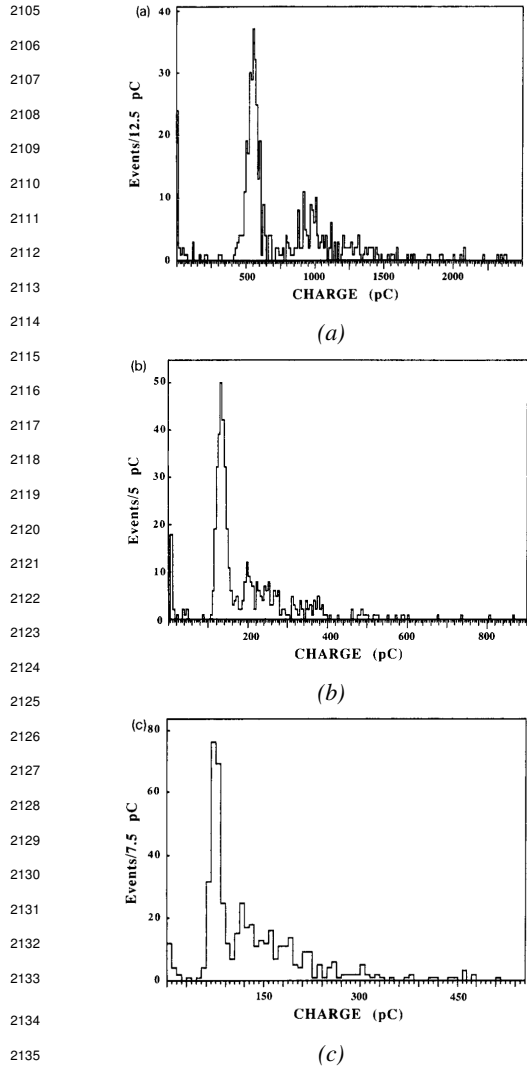


Figure 3.4: Rate capability comparison for the streamer and avalanche mode of operation. An order of magnitude in rate capability for a maximal efficiency drop of 10% is gained by using the avalanche mode over the streamer mode.

2104 **3.2.2 Standard gas mixture for RPCs operated in collider experiments**



2136 *Figure 3.5: Comparison of the charge distribution of*  
 2137 *signals induced by cosmic muons in an RPC operated*  
 2138 *with a gas mixture of argon, butane and bromotrifluo-*  
 2139 *rromethane (CF<sub>3</sub>Br). The Ar/C<sub>4</sub>H<sub>10</sub> is kept constant*  
 2140 *at 60/40 in volume while the total amount of CF<sub>3</sub>Br in*  
 2141 *the mixture is varied: 0% (a), 4% (b) and 8% (c) [184].*  
 2142 *Differences between narrow and wide gaps will be later*  
 2143 *discussed in Section 3.2.3. With CF<sub>3</sub>Br having*  
 2144 *a high GWP, C<sub>2</sub>H<sub>2</sub>F<sub>4</sub> was preferred over it as it was*  
 2145 *considered a more suitable ecofriendly gas in*  
 2146 *the middle of the 90s. An advantage of this new Freon*  
 2147 *component is that it features a high primary*  
 2148 *ionization and a low operating voltage, as reported by* Cardarelli et al. [183]. Thus, the new gas mixtures used were mainly composed of C<sub>2</sub>H<sub>2</sub>F<sub>4</sub> alone with lower content of i-C<sub>4</sub>H<sub>10</sub> in order to reduce the flammability of the mixtures for safety reasons. Performance and models about such mixtures were discussed in papers of Abbrescia et al. [185, 186] and showed a better suitability of

The first RPC working in streamer mode was operated with a 50/50 mixture of argon and butane [178], a standard mixture used at that time in multi-wire proportional chambers. This mixture takes profit of the good effective Townsend coefficient of argon to maximize the number of primary charge carriers freed in the gas by ionizing particles and of the quenching properties of butane. The Townsend coefficient of a gas tells about the multiplication and attachment of primary ionization electrons and will be discussed in Section 3.3.3. Before the discovery of the avalanche mode of RPC operation, the rate capability of RPCs operated in streamer mode was a concern. A possible performance improvement of the detectors could be achieved through the increase of fast charge ratio in the signal development, decreasing the charge induced per avalanche. As it can be seen through Figure 3.5, this effect was studied by adding fractions of Freon-based quenchers, such as CF<sub>3</sub>Br, into the typical Ar/C<sub>4</sub>H<sub>10</sub> gas mixture and showed that a lower induced charge could lead to an improvement the rate capability [184]. This consideration led to the discovery of the avalanche mode which confirmed that the smaller the induced charge, the better the rate capability of the RPCs [181].

From this moment onward, more and more studies were conducted in order to find a gas mixture that would allow for the best suppression of streamers for the benefit of low charge avalanches. Most R&D groups working with narrow gaps started using Freon-based gas mixtures while users of wide gap RPCs kept using Ar/CO<sub>2</sub> based mixtures. The differences between narrow and wide gaps will be later discussed in Section 3.2.3. With CF<sub>3</sub>Br having a high GWP, C<sub>2</sub>H<sub>2</sub>F<sub>4</sub> was preferred over it as it was considered a more suitable ecofriendly gas in the middle of the 90s. An advantage of this new Freon component is that it features a high primary ionization and a low operating voltage, as reported by Cardarelli et al. [183]. Thus, the new gas mixtures used were mainly composed of C<sub>2</sub>H<sub>2</sub>F<sub>4</sub> alone with lower content of i-C<sub>4</sub>H<sub>10</sub> in order to reduce the flammability of the mixtures for safety reasons. Performance and models about such mixtures were discussed in papers of Abbrescia et al. [185, 186] and showed a better suitability of

such a gas mixture with respect to Argon-based ones for operations with high radiation backgrounds requiring high-rate capable detectors, as can be seen from Figures 3.6 and 3.7. Indeed, although the operating voltage of a Freon-based mixture is higher than that of an Argon-based mixture, the efficiency under irradiation is more stable, the voltage range with negligible streamer probability is much wider, and the fast charge ratio available is much greater, providing with more stable operation of the detector.

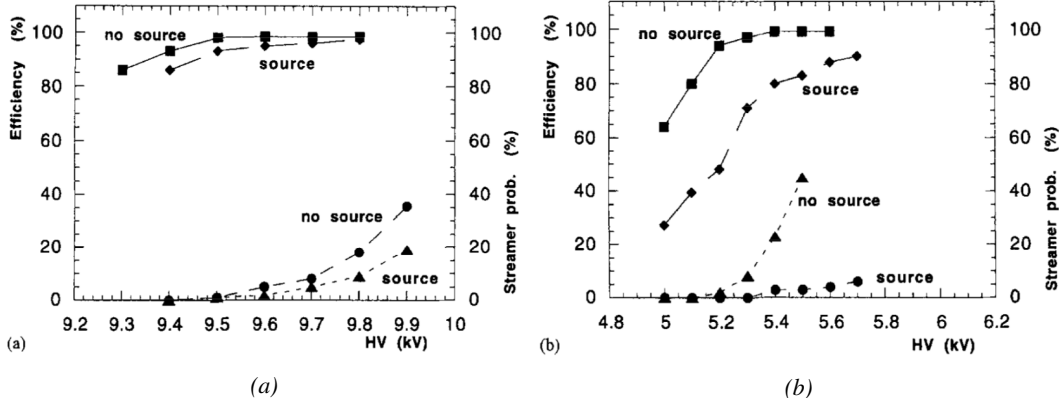


Figure 3.6: Comparison of the efficiency and streamer probability, defined as the fraction of events with an induced charge 10 times larger than that of the average avalanche, with and without irradiation by a 24 GBq  $^{137}\text{Cs}$  source of an RPC successively operated with a 90/10 mixture  $\text{C}_2\text{H}_2\text{F}_4/\text{i-C}_4\text{H}_{10}$  (a) and a 70/5/10/15 mixture of  $\text{Ar}/\text{i-C}_4\text{H}_{10}/\text{CO}_2/\text{C}_2\text{H}_2\text{F}_4$  (b) [185].

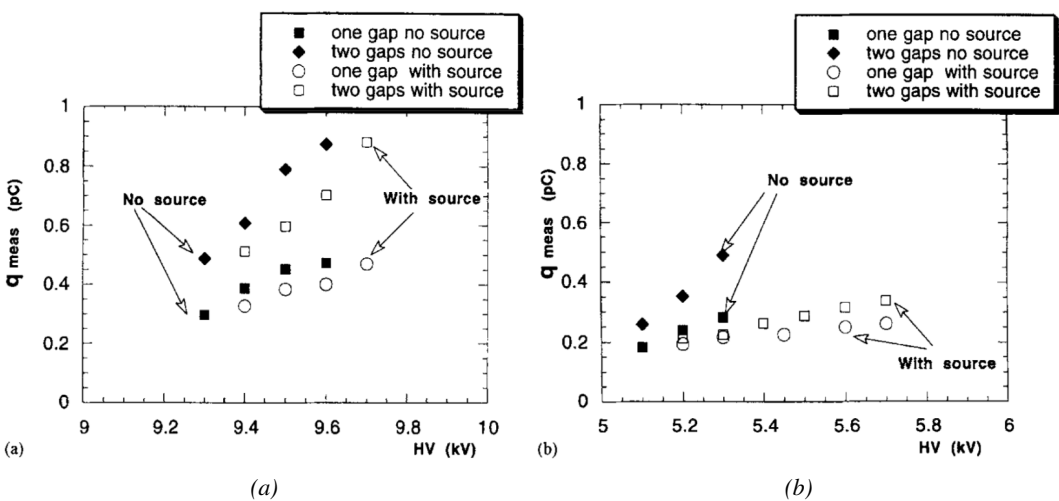


Figure 3.7: Comparison of the fast charge ratio with and without irradiation by a 24 GBq  $^{137}\text{Cs}$  source of an RPC successively operated with a 90/10 mixture  $\text{C}_2\text{H}_2\text{F}_4/\text{i-C}_4\text{H}_{10}$  (a) and a 70/5/10/15 mixture of  $\text{Ar}/\text{i-C}_4\text{H}_{10}/\text{CO}_2/\text{C}_2\text{H}_2\text{F}_4$  (b). The results are provided for both single-gap and double-gap operation [185].

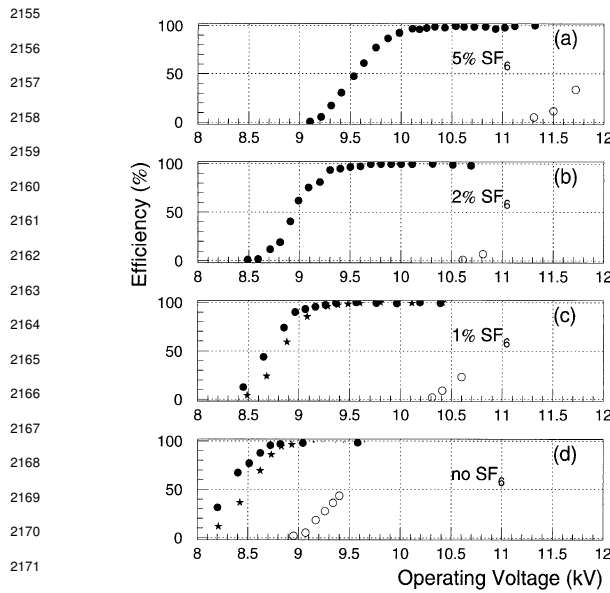


Figure 3.8: Efficiency (circles and stars with 30 mV and 100 mV thresholds respectively) and streamer probability (opened circles) as function of the operating voltage of a 2 mm single-gap HPL RPC flushed with a gas mixture containing (a) 5%, (b) 2%, (c) 1% and (d) no SF<sub>6</sub> [187].

It was later found that the streamers could be further suppressed by adding an electronegative compound into the gas mixture. The benefits of adding SF<sub>6</sub> in order to push the transitions from avalanche to streamers towards high voltages has been discussed in 1998 [187, 188]. Eventually, the high-rate RPC destined to be used in accelerator-based experiments would unanimously start using this compound into their gas mixtures. Being able to control the creation of streamers allows for slower ageing of the detector and lower power consumption as the currents going through the electrodes following the induced charges are smaller. Research is being conducted into new more ecofriendly gas mixture using gases with a much lower Global Warming

Potential. Nonetheless, the typical gas mixture with which RPCs are operated is generally composed of the following 3 gas compounds:

- Tetrafluoroethane (C<sub>2</sub>F<sub>4</sub>H<sub>2</sub>), also referred to as *Freon* or R134a, is the principal compound of the RPC gas mixtures, with a typical fraction above 90%. It is used for its high effective Townsend coefficient and the large average fast charge that allows to operate the detector with a high threshold compared to Argon, for example, that has a similar effective Townsend coefficient but suffers from a lower fast charge. To operate with similar conditions, argon would require a higher electric field leading to a higher fraction of streamers, thus limiting the rate capability of the detector [185, 186].
- Isobutane (i-C<sub>4</sub>H<sub>10</sub>), only present in a few percent in the gas mixtures, is used for its UV quenching properties [200] helping to prevent streamers due to UV photon emission during the avalanche growth.
- Sulfur hexafluoride (SF<sub>6</sub>), is used in very little quantities for its high electronegativity. Any excess of electrons is absorbed by the compound, and streamers are suppressed [187, 188]. Nevertheless, a fraction of SF<sub>6</sub> higher than 1% will not bring any extra benefice in terms of streamer cancelation power but will lead to higher operating voltage [187], as can be understood from Figure 3.8.

Nevertheless, the European Commission adopted a new "F-gas regulation" in 2014 [201] with the goal to strongly control and reduce the use of fluorinated gases with high Global Warming Potential (GWP). As potential replacement for tetrafluoroethane was proposed the trifluoriodomethane

( $CF_3I$ ), a molecule with similar properties than  $CF_3Br$  which was replaced by the tetrafluoroethane, and the 1,3,3,3-tetrafluoropropene ( $C_3H_2F_4$  or HFO-1234re), a molecule with similar properties than the actual tetrafluoroethane and proposed as a replacement in refrigerating and air conditioning systems [202]. These two gases have stronger quenching properties than  $C_2H_2F_4$  which means a much stronger electric field needs to be applied on the parallel electrodes of the RPCs in order to reach full efficiency. But the power supply system of most experiments involving RPCs would not be adapted to such high voltages. But a reduction of the working voltage can be achieved by mixing the potential replacements together with  $CO_2$  [177, 203]. Introducing carbon dioxide into the mixture while keeping similar levels of isobutane and  $SF_6$  increases the streamer probability and the best candidate identified for a compromise in between low enough working voltage and acceptable levels of streamers corresponds to a mixture containing 50% of HFO, 4.5% of  $iC_4H_{10}$ , 0.3% of  $SF_6$  and 45.2% of  $CO_2$  but is not yet considered satisfactory. On the other hand, no good replacement for  $SF_6$  has yet been identified. With its very high Global Warming Potential (23900), even small fractions of this gas in the mixture substantially increase the danger for the environment. Although finding a replacement for this gas is less critical than for the tetrafluoroethane composing more than 90% of usual RPC standard mixtures, the problem will need to be addressed.

### 3.2.3 Detector designs and performance

Different RPC designs have been used, each of them presenting its own advantages. Historically, the first type of RPC that was developed is what is now referred to as *narrow gap* RPC [178, 204].

After the avalanche mode was discovered [181], it has been shown that increasing the width of the gas gap leads to higher rate capability, due to lower charge deposition per avalanche, and lower power dissipation [204], as is shown in Figures 3.9 and 3.10. With the distance in between the electrode being larger, a weaker electric field can be applied, and a lower gain is used as a longer gas volume will contribute to the signal induction on the read-out circuit. Nevertheless, by increasing the gas gap width, the time resolution of the detector decreases. This is a natural result if the increase of active gas volume in the detector is taken into account. Indeed, for a given detection threshold on the induced charge per signal, only the small fraction of gas closest to the cathode will provide enough gain to have a detectable signal. In the case of a wider gas volume, the active region is then larger and a larger time jitter is introduced with the variation of starting position of the avalanche, as discussed in [189] and shown in Figure 3.11.

To improve both the time resolution and the rate capability, different methods were used starting from the middle of the 90s, trying to take advantage of both narrow and wide gap RPCs into a single design. Double-gap RPCs combine two narrow gaps into a single detector to increase the effective sensitive volume. Multigap RPCs in which the large volume a wide gap RPC is divided into thinner

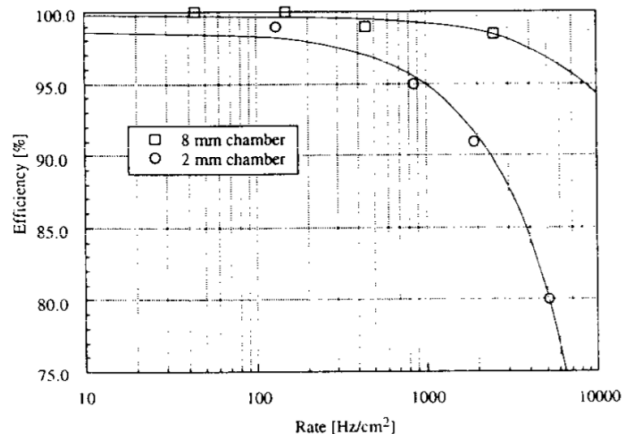
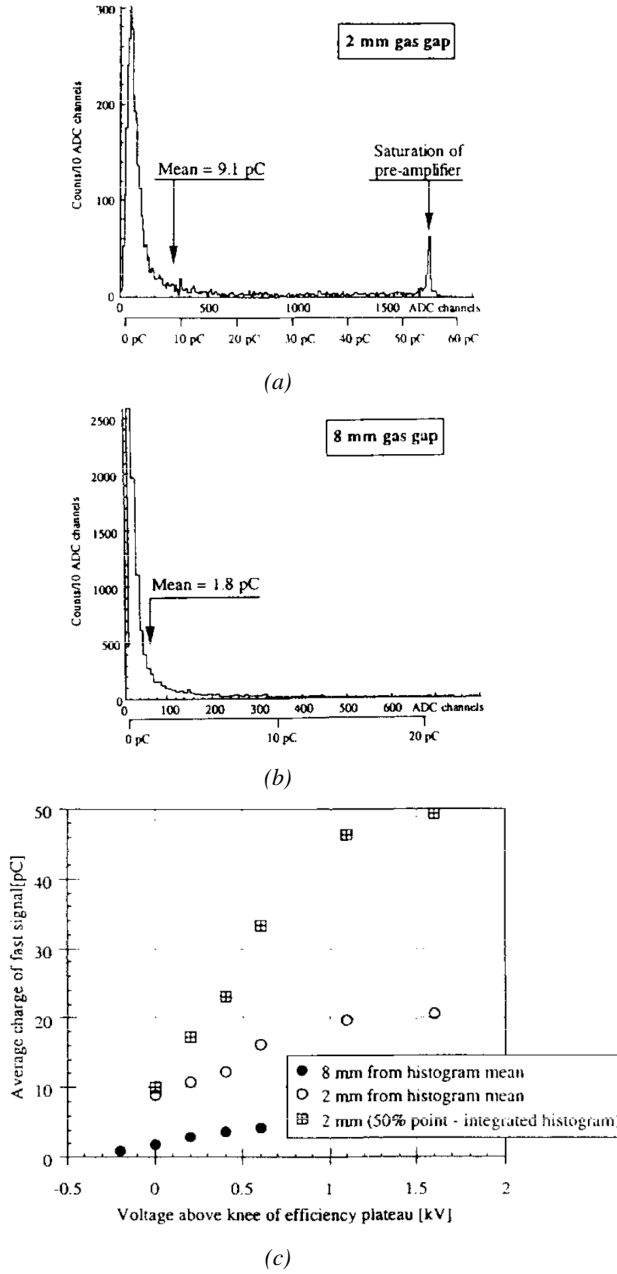
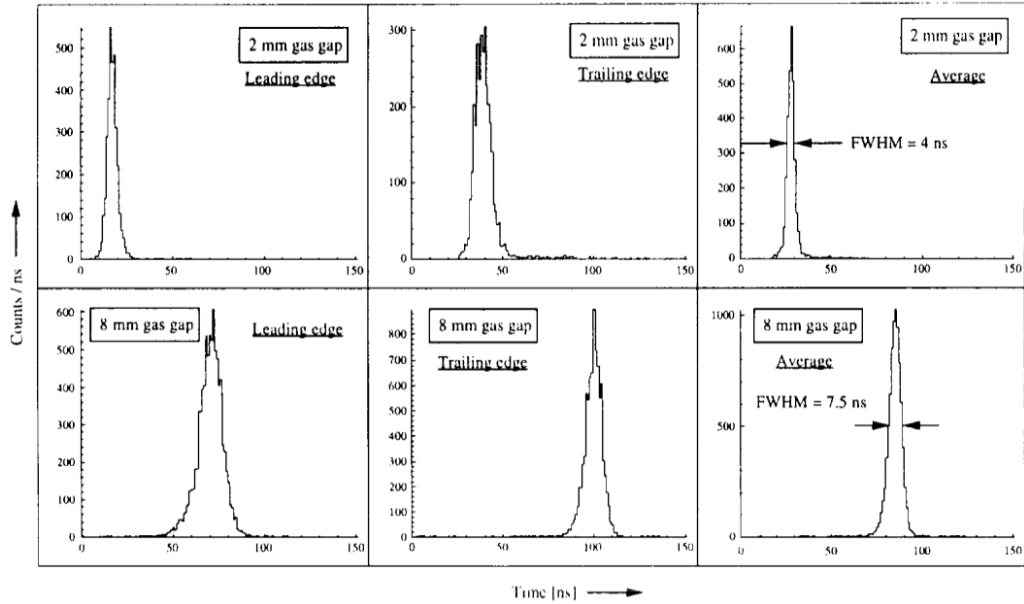


Figure 3.9: Comparison of the rate capability of 8 mm and 2 mm wide RPCs. The lines are linear fits on the data [204].

sub-gaps by adding intermediate electrodes in between the cathode and anode, were developed to improve the time resolution by mimicking narrow gap RPCs.



*Figure 3.10: Distributions of the induced charge of fast signals on 2 mm (a) and 8 mm (b) RPCs exposed to a radiation rate of  $100 \text{ Hz/cm}^2$ . Average induced charge of fast signals as a function of the high voltage applied on 2 mm and 8 mm RPCs (c). In the case of the 2 mm RPC, a saturation of the pre-amplifier was observed. The average of the distribution is underestimated, and the median is shown together with the average to account for this bias [204].*



*Figure 3.11: Time distributions of the leading, trailing, and average of both leading and trailing edges for 2 mm (top row) and 8 mm (bottom row) RPCs exposed to a  $100 \text{ Hz/cm}^2$  radiation rate. The data were collected with RPCs operated at the voltage corresponding to the knee of the efficiency distribution, defined as the point where 95% of the maximum efficiency is obtained [204].*

### 2244 3.2.3.1 Double-gap RPC

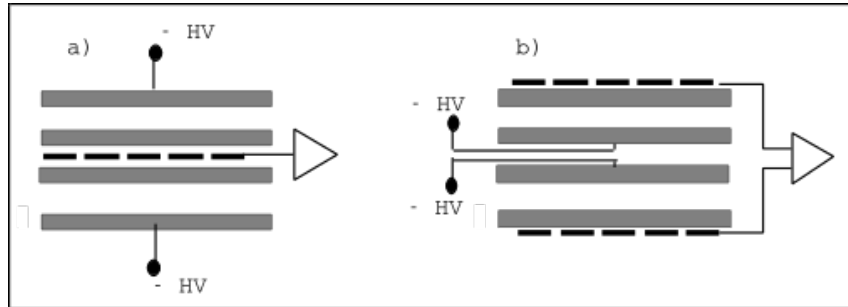


*Figure 3.12: Possible double-gap RPC layouts: a) "standard" 1D double-gap RPC, as used in the CMS experiment, where the anodes are facing each other and a 1D read-out plane is sandwiched in between them, b) double read-out double-gap RPC as used in ATLAS experiment, where the cathodes are facing each other and 2 read-out planes are used on the outer surfaces. This last layout can offer the possibility to use a 2D reconstruction by using orthogonal read-out planes.*

2245 Made out of two narrow RPC detectors stacked on top of each other as shown in Figure 3.12, this  
 2246 detector layout, popularized by the CMS [192] and ATLAS [193] LHC experiments, can be used  
 2247 as an OR system in which each individual chamber participates in the output signal and increases  
 2248 the overall sensitive volume of the detector apparatus. Keeping the copper strip read-out system at  
 2249 ground potential, CMS and ATLAS, with different goals in mind, have chosen different designs as

2250 CMS RPCs possess a 1D read-out while ATLAS RPCs offer a 2D read-out. The difference comes  
 2251 from either placing the read-out in between the gaps with the anodes facing each other, or both RPC  
 2252 gaps in between two layers of read-out panels, one along the X-axis and one along the Y-axis with  
 2253 the cathodes facing each other.

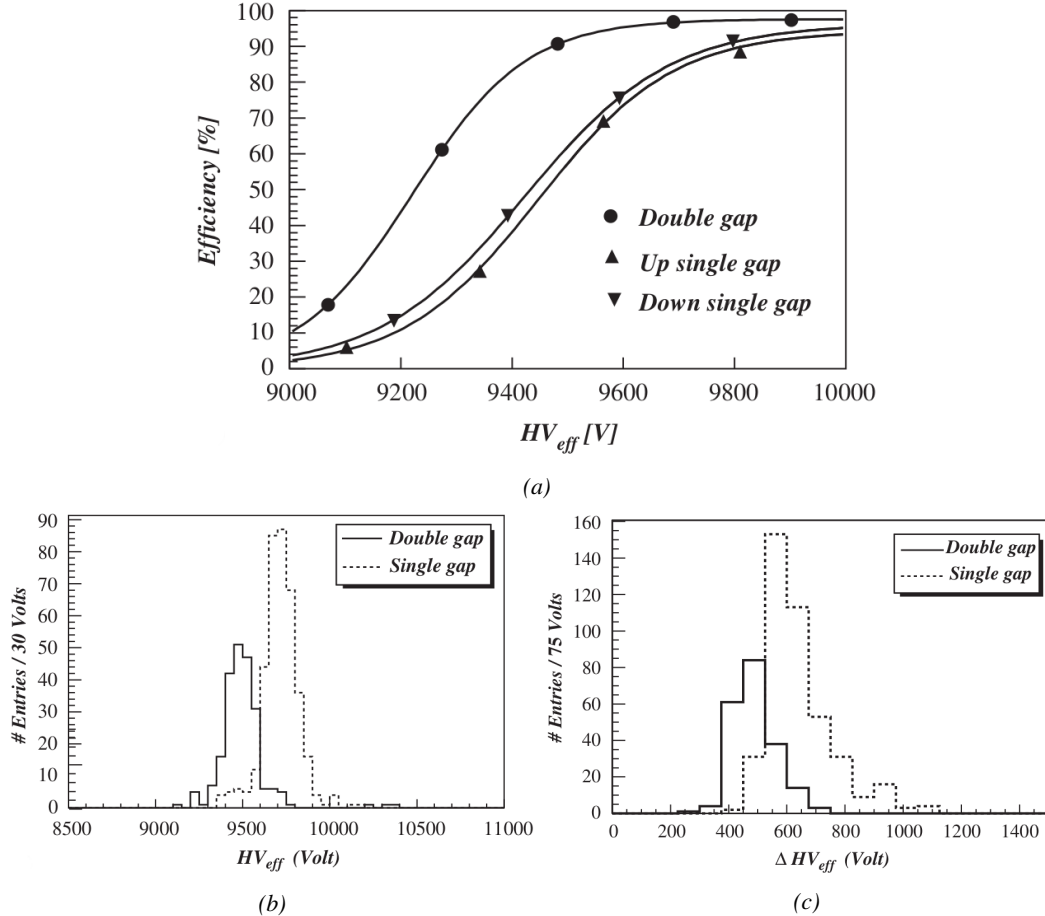


Figure 3.13: Comparison of performance of CMS double and single-gap RPCs using cosmic muons [205].  
 (a): Comparison of efficiency curves. (b): Voltage distribution at 95% of maximum efficiency. (c): Distribution of the voltage difference between the point at 90% and 10% efficiency  $\Delta_{10\%}^{90\%}$ .

2254 The gain of such a detector is reduced by a factor 2 with respect to single-gap RPCs with an effi-  
 2255 ciency plateau reached at lower voltage, as visible on Figure 3.13, due to the two gas gaps contribut-  
 2256 ing to the signal formation and offering a dynamic range, the voltage range between the reaching of  
 2257 the efficiency plateau and the start of streamers, closer to that of a wide gap RPC. A double-gap is  
 2258 then fully efficient while the individual RPC gaps composing it are only 70 to 80% efficient. Nat-  
 2259 urally, by operating the double-gap at a lower voltage, the rate capability increases as the induced  
 2260 charge per gap is decreased with respect to a single-gap detector also leading to a reduction of the  
 2261 streamer probability and a better extraction of the fast charge of the total signal as was shown already  
 2262 in Figure 3.7.

2263 **3.2.3.2 Multigap RPC (MRPC)**

2264 MRPCs have a design in which floating sub  
 2265 electrode plates are placed into a wide gap  
 2266 RPC to divide the gas volume and create a sum  
 2267 of narrow gaps [189, 190]. Similarly to the  
 2268 double-gap RPC for which the gain could be  
 2269 reduced by increasing the dynamic range, the  
 2270 multigap reduces the gain while keeping a total  
 2271 dynamic range similar to that of a wide gap  
 2272 RPC by reducing the size of each individual  
 2273 sub-gap composing the detector. The dynamic  
 2274 range, associated to the sensitive volume, and  
 2275 the comparison of each detector layout to the  
 2276 wide gap RPC is shown in Figure 3.14.

2277 By operating the detector with thinner  
 2278 gaps, its time resolution is improved. Similarly  
 2279 to the time resolution presented in Figure  
 2280 3.11 for the wide gap RPC of 8 mm,  
 2281 a complementary study was conducted on  
 2282 multi-gap RPCs using two 4 mm and four  
 2283 2 mm subgaps. As shown in Figure 3.15,  
 2284 an improvement of the time resolution with  
 2285 the reduced gap width and increased number  
 2286 of gaps, keeping the same total sensitive  
 2287 volume [190].

2288 After the problem of streamers was solved  
 2289 by adding  $SF_6$  into the gas mixture, the size of  
 2290 the MRPCs decreased as the research groups  
 2291 started applying the concept to the narrow gap  
 2292 RPCs leading to the now widely used micro-  
 2293 gap MRPCs. The time resolution of such a  
 2294 detector can reach of few tens of ps, with  
 2295 gas gaps of the order of a few hundred  $\mu m$   
 2296 as shown in Figure 3.16 representing a single  
 2297 cell of ALICE Time-of-flight (ToF) system consisting of double MRPCs, as studied in the early  
 2298 2000s [206].

2299 The MRPC is mainly used as ToF detector [206–210] due to its excellent timing properties that  
 2300 allows performing particle identification as explained by Williams in [211]. The principle of particle  
 2301 identification using ToF consists in the measurement of the velocity of a particle. Indeed, particles  
 2302 are defined by their mass (which is the parameter of interest here, assuming e.g. that their electric  
 2303 charge being measured using the bending angle of the particles traveling through a magnetic field)  
 2304 and this mass can be calculated by measuring the velocity  $\beta$  and momentum  $p$  of the particle:

$$(3.3) \quad \beta = \frac{p}{\sqrt{p^2 + m^2}}$$

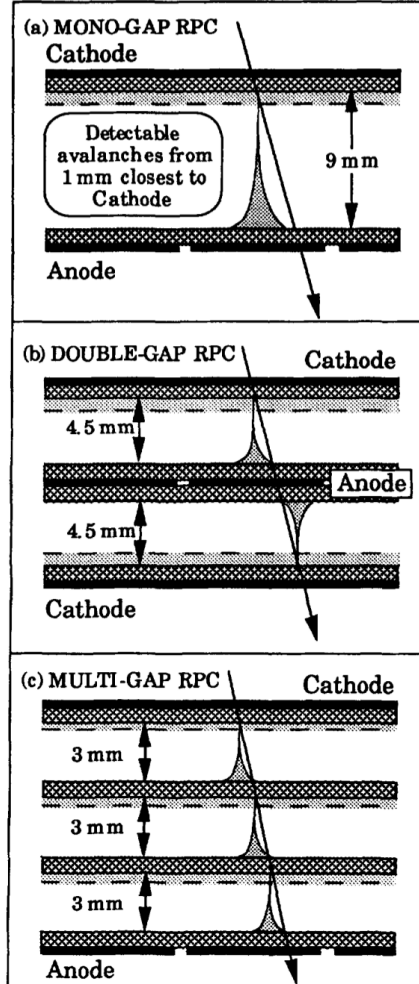
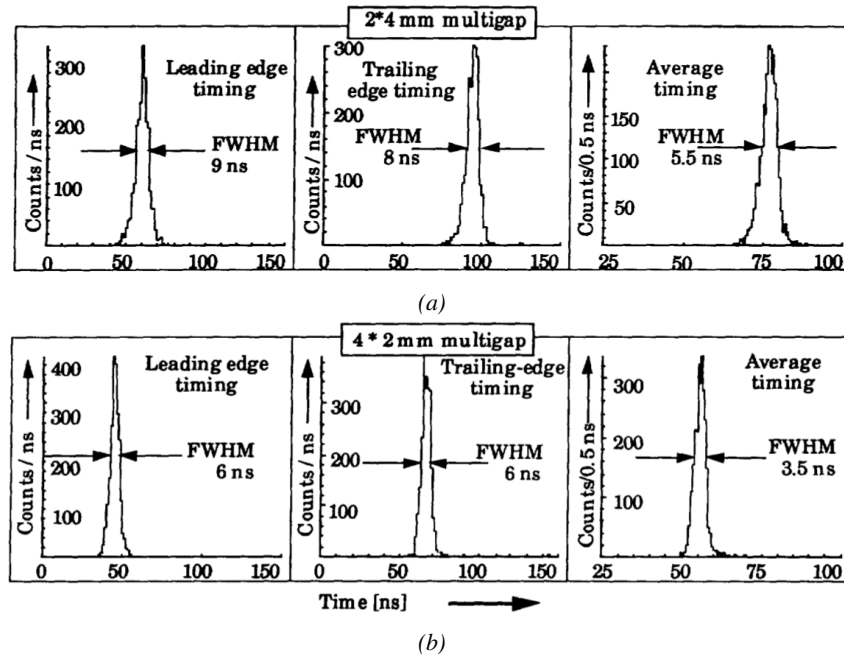
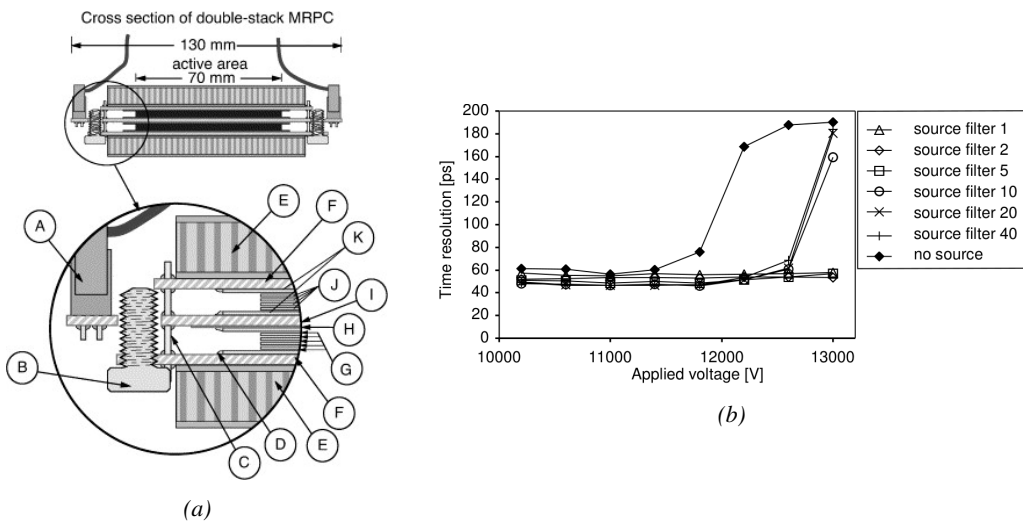


Figure 3.14: Representation of different RPC layouts (wide gap (a), double-gap (b) and multigap (c)), of the corresponding sensitive volume in gray, and of the associated avalanche size [190].



*Figure 3.15:* Time distributions of the leading, trailing, and average of both leading and trailing edges for multigap RPCs consisting in two 4 mm (a) and four 2 mm (b) exposed to a  $100 \text{ Hz/cm}^2$  radiation rate. The data were collected with RPCs operated at the voltage corresponding to the knee of the efficiency distribution, defined as the point where 95% of the maximum efficiency is obtained [190].



*Figure 3.16:* Presentation of a study for an ALICE MRPC cell prototype using  $250 \mu\text{m}$  gas gaps,  $620 \mu\text{m}$  outer glass electrodes, and  $550 \mu\text{m}$  inner floating electrodes (a), and of its time resolution performance as a function of the applied high voltage for different radiation levels corresponding to different filter settings of the  $740 \text{ GBq}$   $^{137}\text{Cs}$  source at the former CERN GIF facility (b) [206].

Intuitively, it is trivial to understand that two different particles having the same momentum will have a different velocity due to the mass difference and thus a different flight time  $T_1$  and  $T_2$  through the detector and this is used to separate and identify particles. The better the time resolution of the ToF system used, the stronger the separation will be:

(3.4)

$$T = \frac{L}{v} = \frac{L}{c \cdot \beta}$$

$$\Delta T = T_1 - T_2$$

$$\begin{aligned} &= \frac{L}{c} \left( \sqrt{1 + m_1^2/p^2} - \sqrt{1 + m_2^2/p^2} \right) \\ &\cong (m_1^2 - m_2^2) \frac{L}{2cp^2} \end{aligned}$$

Taking into account the distortion effect on the electric field inside of an MRPC built using micro gaps due to the exposition to irradiation, distortion that can be understood by monitoring the current drawn by the detector which should stay constant at a constant electric field, another benefice of using such small gas gaps is the strong reduction of the average avalanche volume and thus of the blind spot on MRPCs leading to an improved rate capability. Multigaps can sustain backgrounds of several kHz/cm<sup>2</sup> as demonstrated in Figure 3.17.

### 3.2.3.3 Charge distribution and performance limitations

A direct consequence of the different RPC layouts is a variation of intrinsic time resolution of the RPC depending on the gap size, and of its rate capability when the deposited charge per event is spread over a larger number of amplification volumes. This allows reducing of the overall gain of the detectors which is compensated by a pre-amplification of the signals at the level of the electronics. In this sense, an advantage is given to multi-gap RPCs with their sub-millimeter gas volumes providing very consistent signals.

From the charge spectrum point of view, each layout has its own advantages. While the double-gap has the highest ratio between the total charge it induces on the read-out and the charge that effectively drifts through its volume, as seen in Figure 3.18, the multigap has a charge spectrum with a maximum significantly above zero, as visible in Figure 3.19. A high induced-over-drifting charge ratio means that the double-gap can be safely operated at a high threshold or that at a similar threshold

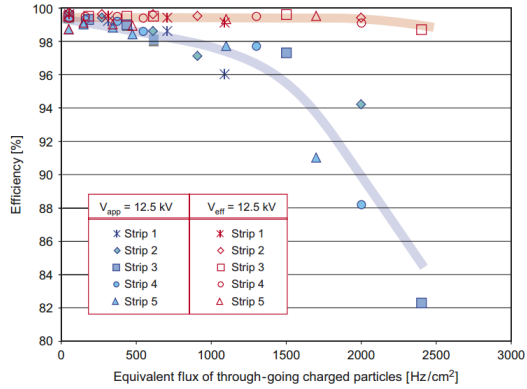


Figure 3.17: Comparison of the detector performance of ALICE ToF MRPC [212] at fixed applied voltage (in blue) and at fixed effective voltage (in red). The effective voltage is kept fixed by increasing the applied voltage according to the current drawn by the detector.

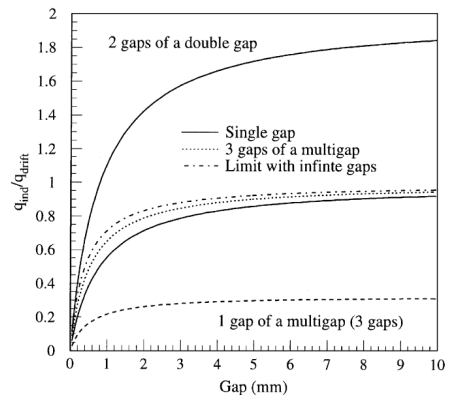
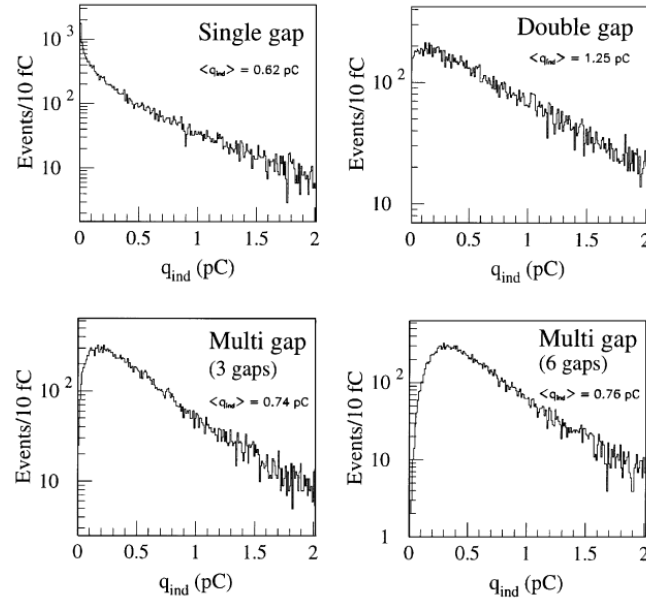


Figure 3.18: Ratio between total induced charge and drifting charge have been simulated for single-gap, double-gap and multigap layouts [213]. The total induced charge for a double-gap RPC is a factor 2 higher than for a multigap.

it can be operated with a twice smaller drifting charge, leading to a higher rate capability if operated with sensitive enough electronics. On the other hand, the strong detachment of the charge spectrum from the origin in the MRPC case allows reaching a higher efficiency with increasing threshold as most of the signals have a higher charge content due to the convolution of several single-gap spectra.

The range of stable efficiency increases with the number of gaps, as presented in Figure 3.20.



*Figure 3.19: Charge spectra have been simulated for single-gap, double-gap and multigap layouts [213]. It appears that while single-gaps show a decreasing spectrum, double and multigap layouts exhibit a spectrum whose maximum is significantly above zero. The shift of maximum value in the spectrum increases along with the number of gaps.*

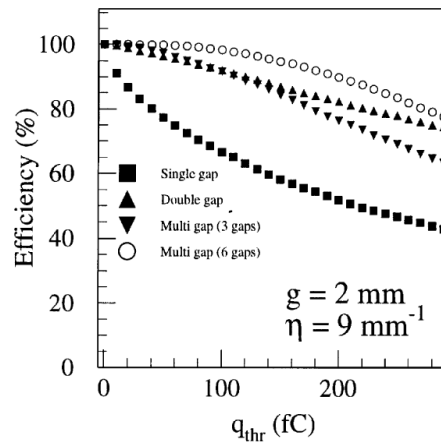


*Figure 3.20: The maximal efficiency theoretical is simulated for single-gap, double-gap and multigap layouts [213] at a constant gap thickness of 2 mm and using an effective Townsend coefficient of 9 mm<sup>-1</sup>.*

<sup>2344</sup> **3.3 Signal formation**

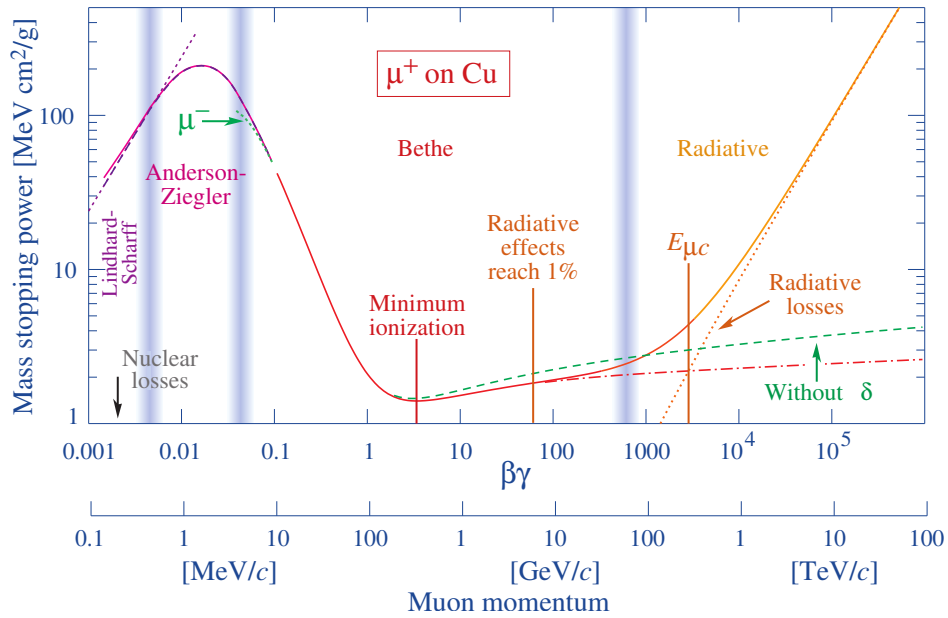


*Figure 3.21: Mass stopping power as a function of  $\beta\gamma = p/Mc$  for positive muons in copper [115]. The total stopping power is indicated with a solid line and local components with dashed lines. The vertical bands are used to indicate boundaries between different approximations used at different energy range.*

<sup>2345</sup> The physics of Resistive Plate Chambers still is far from fully understood and many attempts are  
<sup>2346</sup> made to describe these detectors using phenomenological models [197, 214, 215]. These theoretical  
<sup>2347</sup> works have led to a better understanding of the key principles that account for RPCs signal formation.  
<sup>2348</sup> As previously discussed, the typical mixture of such a detector is to a large extent composed by a  
<sup>2349</sup> gas with some quenching properties and a low ionization potential to easily produce electrons, with  
<sup>2350</sup> the addition of UV quencher and electronegative compounds. The electronic avalanche formation  
<sup>2351</sup> will be triggered by a charged particle passing through the gas, typically a muon in the case of  
<sup>2352</sup> most applications involving RPCs. The production of electrons in the gas of a detector is related  
<sup>2353</sup> to the energy lost by the incoming particle traveling through a material medium. The example of  
<sup>2354</sup> the mass stopping power of copper on muons is given in Figure 3.21 on which the different energy  
<sup>2355</sup> loss mechanisms at different energy ranges are visible. Once primary ionization electrons have been  
<sup>2356</sup> freed in the gas volume, the electric field applied in between the electrodes of the RPC will make the  
<sup>2357</sup> charges move and there will be a competition in the gas in between the Townsend and attachment  
<sup>2358</sup> coefficient which describe the evolution of the number of electrons in an avalanche. While drifting  
<sup>2359</sup> through the gas, the electrons are also subjected to diffusion that will affect the evolution of the  
<sup>2360</sup> avalanches. Finally, when the avalanche is big enough, the accumulation of negative (electrons) and  
<sup>2361</sup> positive (ions) charges in the gas volume will start affecting the local electric field. This effect is  
<sup>2362</sup> known as the *space charge effect*.

### 3.3.1 Energy loss at intermediate energies

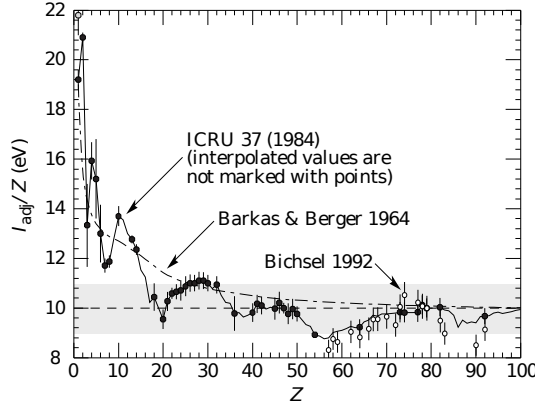


Figure 3.22: Mean excitation energies normalized to the atomic number as adopted by the ICRU [115, 216, 217].

A particle traveling through a medium will interact with its components, losing energy. When a muon travels through the gas of a gaseous detector, at the energy range usually observed, typically of the order of a few GeV for cosmic muons[115] to a few hundreds of GeV in accelerators such as the LHC, it interacts with the molecules of the gas leading to dissipation of the transferred energy in the form of inelastic scattering or ionization. The photons and electron-ion pairs resulting from these interactions can trigger avalanches in the gas which will contribute to feed the avalanche growth thanks to the strong electric field applied in between the two electrodes of an RPC.

At higher energies, the energy loss through

photon radiation can't be neglected anymore as can be seen in Figure 3.21.

The mass stopping power of moderately relativistic ( $0.1 \lesssim \beta\gamma \lesssim 1000$ ) heavy particles ( $M \gg m_e$ ) traveling through a medium via excitation and ionization processes was studied by Bethe in 1930 [218] and is well described by the so called the Bethe Formula given in Equation 3.5.

$$(3.5) \quad \left\langle -\frac{dE}{dx} \right\rangle = K z^2 \frac{Z}{A} \frac{1}{\beta^2} \left( \frac{1}{2} \ln \frac{2m_e c^2 \beta^2 \gamma^2 W_{max}}{I^2} - \beta^2 - \delta(\beta\gamma) \right)$$

The different parameters used in this equation are

$E$	- incident particle energy $\gamma Mc^2$	MeV
$x$	- mass per unit area	$\text{g cm}^{-2}$
$N_A$	- Avogadro's number	$6.022\ 140\ 857(74) \times 10^{23} \text{ mol}^{-1}$
$c$	- speed of light in vacuum	$299\ 792\ 458 \text{ m s}^{-1}$
$\mu_0$	- permeability of free space	$4\pi \times 10^{-7} \text{ N A}^{-2}$
$\epsilon_0$	- permittivity of free space $\epsilon_0 = 1/\mu_0 c^2$	$8.854\ 187\ 817 \dots \times 10^{-12} \text{ F m}^{-1}$
$\alpha$	- fine structure constant $\alpha = e^2/4\pi\epsilon_0\hbar c$	$1/137.035\ 999\ 139(31)$
$r_e$	- classical electron radius $r_e = e^2/4\pi\epsilon_0 m_e c^2$	$2.817\ 940\ 3227(19) \text{ fm}$
$e$	- elementary charge of the electron	$-1.6021766208(98) \times 10^{-19} \text{ C}$
$m_e c^2$	- electron mass $\times c^2$	$0.510\ 998\ 9461(31) \text{ MeV}$
$K$	- constant defined as $K = 4\pi N_A r_e^2 m_e c^2$	$0.307\ 075 \text{ MeV mol}^{-1} \text{ cm}^2$
$z$	- charge number of incident particle	
$Z$	- atomic number of absorbing medium	
$A$	- atomic mass of absorbing medium	$\text{mol}^{-1}$
$\beta$	- velocity of particle $\beta = v/c$	
$\gamma$	- Lorentz factor $\gamma = (1 - \beta^2)^{-1/2}$	
$W_{max}$	- maximum energy transfer through a single collision	MeV
$I$	- mean excitation energy of absorbing medium	eV
$\delta(\beta\gamma)$	- density effect correction to ionization energy loss	

In this equation, the maximum energy transfer  $W_{max}$  is defined as function of the incident particle mass  $M$  expressed in MeV/c<sup>2</sup>:

$$(3.6) \quad W_{max} = \frac{2m_e c^2 \beta^2 \gamma^2}{1 + 2\gamma m_e/M + (m_e/M)^2}$$

and the mean excitation energy  $I$  depends on the absorber. Its determination is non-trivial, but recommendations are given by the International Commission on Radiation Units & Measurements (ICRU) based on experimental measurements and interpolations as shown in Figure 3.22.

For the case of copper, the mean stopping power is visible in Figure 3.21. The mean stopping power corresponding only to the Bethe range for other materials is given in Figure 3.23 and shows that  $\langle -dE/dx \rangle$  is similar for each material with a slow decrease with  $Z$ .

The factor affecting the equation the most is  $\beta$ . Indeed, the dependence on  $M$  is introduced at higher energies in the logarithm via the max transfer energy per single collision. In most practical cases, only the dependence on  $\beta$  is considered as most of the relativistic particles are closed to the lowest mean energy loss rate and are referred to as minimum ionizing particles (mip's). The almost logarithmic relation between the mean energy loss rate for minimum ionizing particles and  $Z$  is shown in Figure 3.24.

Finally, the term  $\delta(\beta\gamma)/2$  in Equation 3.5 corresponds to the density effect correction introduced to account for the polarization of a real media that limits the spatial extension of the electric field of relativistic particles. As the energy of a particle increases, the associated electric field will flatten and extend. Due to this effect, the distant collision contribution to Equation 3.5 will increase as  $\ln(\beta\gamma)$  but the polarization of the media truncates this rise.

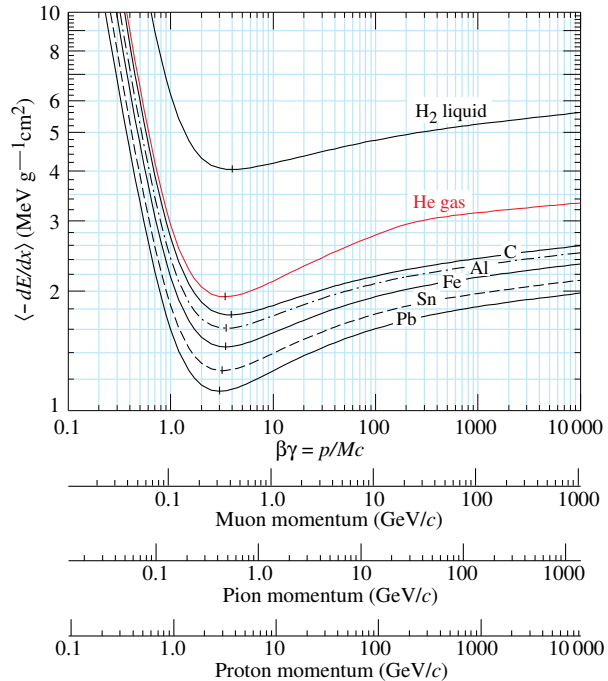


Figure 3.23: Mean mass stopping power for liquid hydrogen, as used in bubble chambers, gaseous helium, carbon, aluminum, iron, tin, and lead without the inclusion of radiative effect at higher  $\beta\gamma$  necessary for pions and muons in denser materials [115].

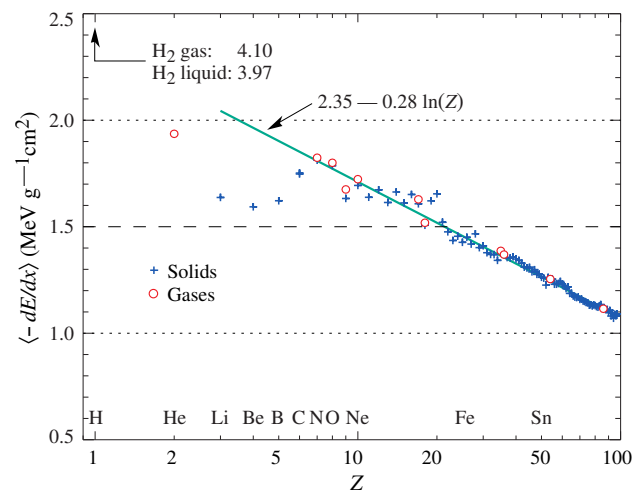


Figure 3.24: Mean mass stopping power at minimum ionization as a function of the atomic number [115].

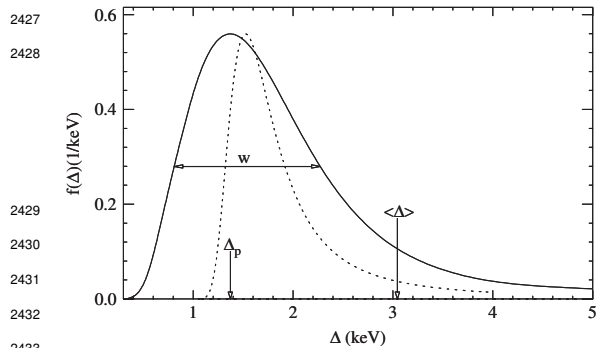


Figure 3.25: Example of straggling function (solid)  $f(\Delta)$  of particles passing through 1.2 cm of Argon gas with a  $\beta\gamma$  of 3.6. The original Landau distribution is shown with a dashed line [219].

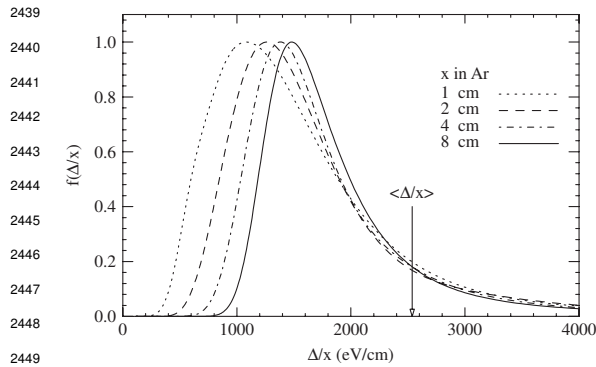


Figure 3.26: Evolution of straggling functions  $f(\Delta)$  of particles passing through a volume of Argon gas with a  $\beta\gamma$  of 3.6 with increasing thickness  $x$  [219].

Thus, the energy loss distribution is better represented by its most probable energy loss  $\Delta_p$  and its full-width-at-half-maximum (FWHM)  $w$ . As showed by Figure 3.26, the distribution is affected by the thickness of the gas volume with the most probable energy loss normalized to the thickness increasing and the width decreasing for increasing thickness, converging towards the Landau distribution, whereas the mean energy loss is unchanged. Corrections to include the electron binding energy and the atomic shell structure are brought to the original Landau equation in order to account better for the number of collisions leading to an increased width of the energy loss distribution [219]. The corrected energy loss distribution is usually referred to as *straggling function*.

In the case of gas mixtures, composed of several elements, using Bragg additivity it can be understood that the mean energy loss of the mixture is the sum of the mean energy losses in each layer of individual element  $j$  of weight fraction in the mixture  $w_j$  [115].

$$(3.8) \quad \left\langle \frac{dE}{dx} \right\rangle = \sum w_j \left\langle \frac{dE}{dx} \right\rangle_j$$

At high energies, the correction is given by Equation 3.7:

$$(3.7) \quad \delta/2 \longrightarrow \ln(\hbar\omega_p/I) + \ln(\beta\gamma) - 1/2$$

where  $\hbar\omega_p$  represents the plasma energy that depends on the electron density of the media and the electron mass and can be calculated as  $\sqrt{\rho(Z/A)} \times 28.816 \text{ eV}$ . The introduction of this correction term reduces the increase of the mean stopping power at higher energies as can be seen in Figure 3.21. Moreover, due to lower electron density, the effect is less visible for gases than for liquids and solids as can be seen in Figure 3.23.

The mean energy loss per collision can be difficult to measure for data samples with low statistics but is not always representative of the energy loss distribution for a given incident particle energy. Hence, it is easier to access the most probable energy loss which is a lower value than the average loss due to the distribution of the energy transfer. This value is well described by a highly skewed Landau distribution for detectors with "moderate" thickness  $x$ , expressed in  $\text{g mol}^{-1}$ . But for gas volumes, a Landau distribution greatly underestimates the width  $w$  of the distribution and only succeeds to provide with a correct value for the most probable energy loss, as shown in Figure 3.25.

2465 **3.3.2 Primary ionization**

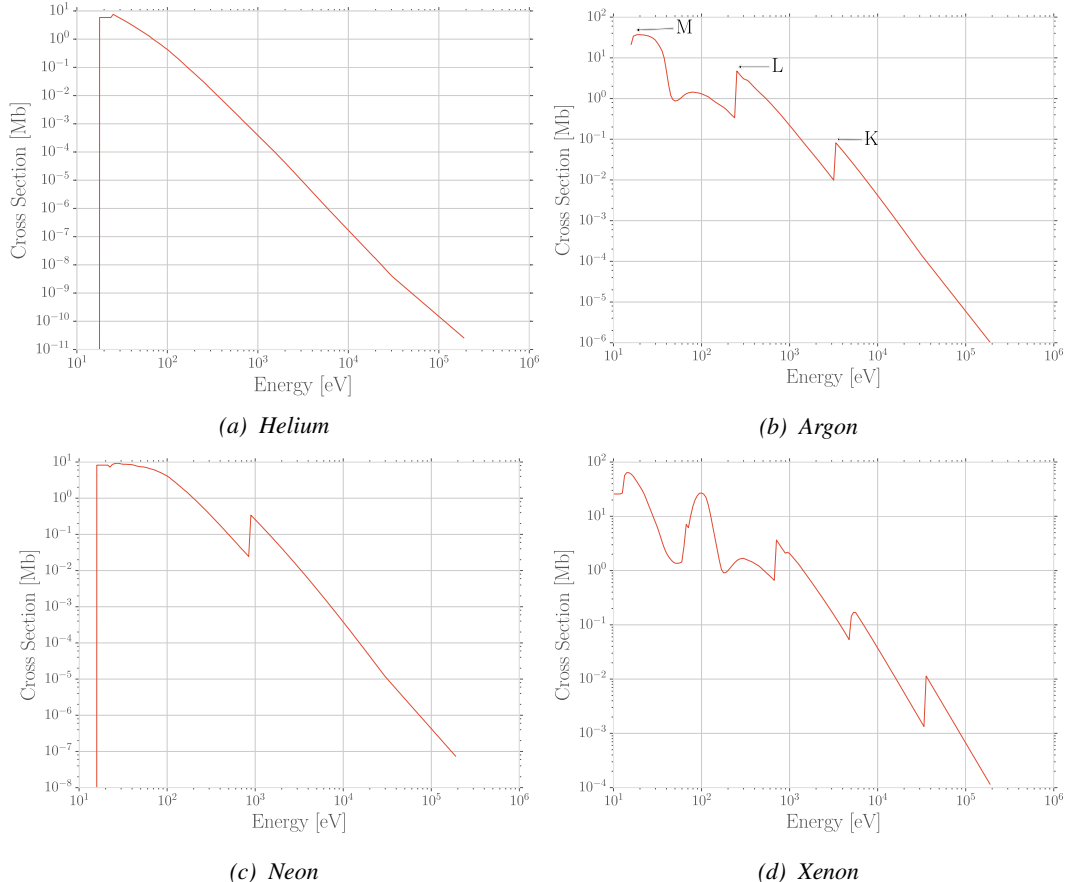


*Figure 3.27: Photoabsorption cross section as computed by HEED for noble gases with different electron shell numbers [215].*

2466 Using the Bethe formula to compute the mean energy transfer of charged particles when traveling  
 2467 through a gas volume may give some feeling on the physics that affect the particle but doesn't provide  
 2468 detailed enough information about the individual ionizations along its tracks at a microscopic level.  
 2469 In order to simulate efficiently an RPC and hence understand the processes governing avalanche  
 2470 creation and growth, knowledge on the ionization process is necessary.

2471 To convert the energy loss rate into a number of primary ionizations, the Photo-Absorption Ionization  
 2472 (PAI) model [220] was developed in 1980. It is based on the cross section of photoionization  
 2473 of gas atoms and the dielectric constant of the medium through which the charged particles are going.  
 2474 Indeed, the interaction of charged particles with the gas molecules, being of electromagnetic  
 2475 nature, is mediated by photons and, hence, the cross section for photoionization is important to understand.  
 2476 This approach is nevertheless semi-classical as it relies on classical electrodynamics. It only gives access to the energy transfer to the gas atoms, and no information on the energy dissipation  
 2477 and secondary emissions is available. The energy transferred to the medium is not all used for  
 2478 ionization.

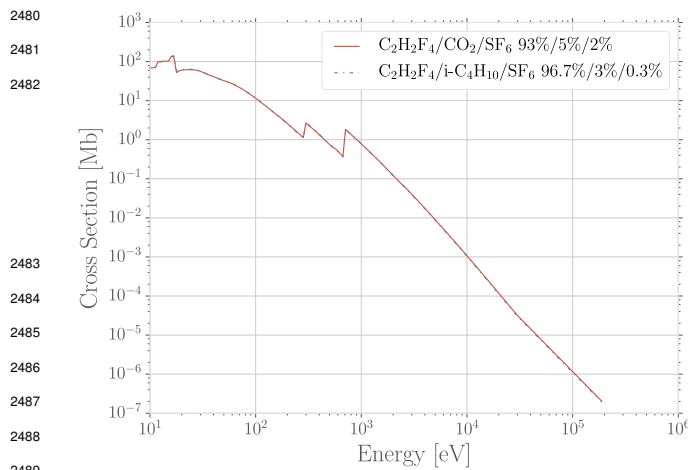


Figure 3.28: Photoabsorption cross section as computed by HEED for typical RPC gas mixtures [215]. The RPC mixture with  $CO_2$  corresponds to the mixture used by CALICE SDHCAL [221] while the other one was foreseen for the experiment ATLAS [222] but has been changed since then. Both mixtures being largely composed of  $C_2H_2F_4$ , the curves are nearly identical.

full atom rather than with a single electron. With the incoming particle interacting with a single electron, the atom is left in an excited state once the photo-electron has been emitted with an energy corresponding to the transferred energy minus the binding energy of the electron shell. The resulting vacancies in the electronic shell will be filled through emission of photons or Auger electrons and can contribute to further ionization or excitation in the gas volume. Fluorescence photons are usually not considered as they only constitute a very small fraction of secondary emissions [224].

Assuming that the transferred energy is absorbed in its totality by a single electronic shell, the PAI model was extended to the new Photo-Absorption Ionisation with Relaxation (PAIR) model [224] to include relaxations. In this model, the cross section corresponding to the whole atom is re-expressed using a sum of partial cross sections corresponding to the different electronic shells. When one or more electrons are knocked out of the atom, the vacancies are filled by electrons of the shell above with relaxation by Auger electron emission. These processes happen in cascade from the inner shell to the outer one until all the vacancies are filled and the energy has been released. This model is included in the program HEED developed at CERN [225] and gets called by Garfield [226], a program developed for the simulation of gaseous detectors. The results for the cross section for a few noble gases are given in Figure 3.27. It can be seen that for each shell, the cross section exhibits an absorption peak. More complex patterns are seen with larger atoms such as Xenon on Figure 3.27d. For gas mixtures, like the typical RPC mixtures, the cross section is shown in Figure 3.28. Both mixtures being mainly composed of  $C_2H_2F_4$ , the variations in between the two cross section profiles are very subtle and depends on the concentration of the other compounds.

Once the interaction cross section is known, it is possible to determine the distribution of energy loss and the number of produced electrons, as shown in Figure 3.29 for Helium, Argon, which is used in gaseous detectors, and for a typical RPC mixture [215]. The distributions are computed using HEED and show typical straggling function profiles with some complex structures that can be related to interaction of the incoming particle with the different electron shells. Helium does not have a large photoabsorption cross-section according to Figure 3.27a and a muon will not likely lose

For an energy deposition  $\Delta$ , the number of electron-ion pairs produced is:

$$(3.9) \quad \Delta = n_i W$$

$W$  corresponds to the average energy per pair production that depends on the medium and is greater than the ionization potential leading to the conclusion that part of the transferred energy is dissipated through other processes [215, 223]. In order to understand the energy dissipation and the secondary emissions, the fine structure of each atom is taken into account. Through the PAI model, the incident charged particle is assumed to interact with the

2522 a lot of energy and create a lot of electrons. In a more complex atom like Argon, the cross-section is  
 2523 larger and will lead to a larger energy loss of muons and more electron produced. Finally, a complex  
 2524 gas mixture used in RPCs will offer an even larger cross-section, a wider energy loss distribution  
 2525 and will be able to produce more electrons. The same information is confirmed by looking at the  
 2526 evolution of the mean number of electron clusters produced along a muon track as a function of  
 2527 the lorentz factor associated to muons shown in Figure 3.30a. The size of these clusters is studied  
 2528 through Figure 3.30b which shows that in most of the cases ( $\approx 80\%$ ) the clusters are only composed  
 2529 of a single electron which is consistent with minimum ionizing particles.

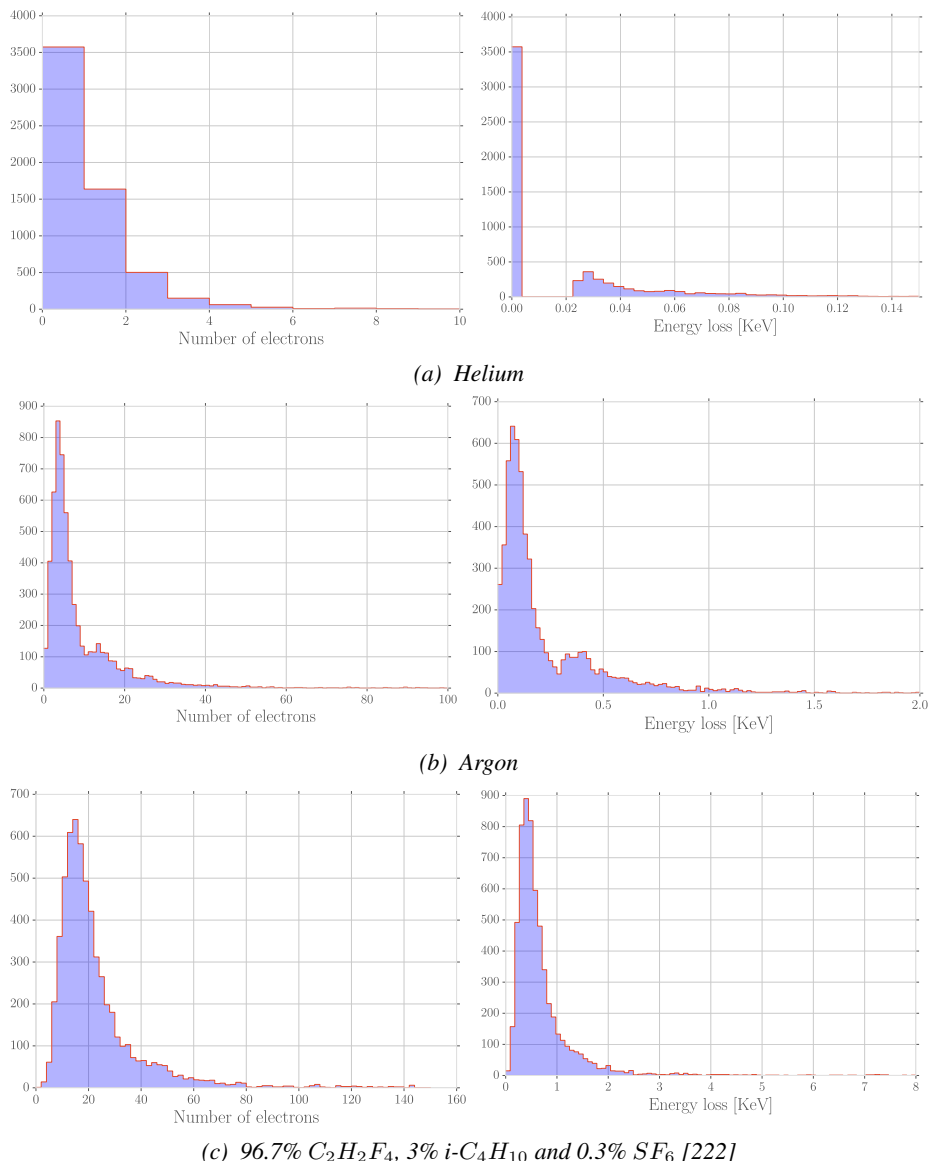


Figure 3.29: Distributions of number of electrons (left) and energy loss (right) for a 5 GeV/c muon passing through 1.2 mm of Helium (a), Argon (b) or a typical RPC gas mixture (c) [215].

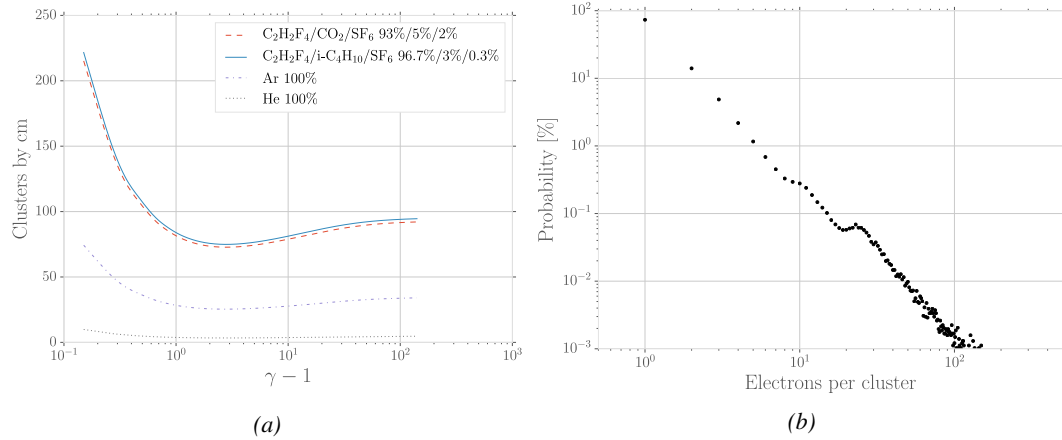


Figure 3.30: (a): Mean cluster density for muons through different gas volumes [215]. (b): Distribution of the number of electrons per cluster for a 5 GeV/c muon traveling through a mixture of 96.7%  $C_2H_2F_4$ , 3%  $i-C_4H_{10}$  and 0.3%  $SF_6$  [215, 222].

### 3.3.3 Development and propagation of avalanches

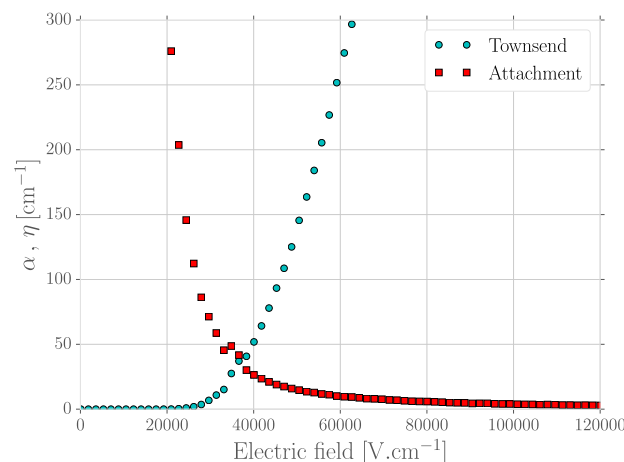


Figure 3.31: Townsend and attachment coefficient for a typical 96.7/3/0.3 mixture of  $C_2H_2F_4/i-C_4H_{10}/SF_6$ , at a temperature  $T = 296.15 \text{ K}$  and a pressure  $P = 1013 \text{ hPa}$  [215, 222].

is reached, the electrons can get attached to a gas molecule instead. These two effects can be described using a simple model in which the multiplication and attachment processes are given by the Townsend coefficient  $\alpha$  and the attachment coefficient  $\eta$ , assuming that the history of previous interactions in the gas does not influence new interactions. This model simply takes into account probabilities to have at the gas depth  $z$ , for a given number  $n$  of free electrons in the gas,  $n + 1$  or  $n - 1$  electrons at the depth  $z + dz$  (respectively  $n\alpha dz$  and  $n\eta dz$ ).

From the clusters released in the gas volume by the charged particles, free electrons will start drifting due to the electric applied in between the electrodes of the RPC. Gaining velocity and energy, these electrons in their turn will be able to ionize the gas. This process being repeated by all the produced electrons will trigger an avalanche to develop.

The growth of the avalanche can be intuitively understood as a competition between two effects. Due to their increasing energy, electrons have a probability to trigger new ionizations by interacting with gas molecules. On the other hand, before the minimal amount of energy

2555 The mean number of electrons  $\bar{n}$  and  
 2556 cations  $\bar{p}$  can be written for single compound  
 2557 gases as

$$(3.10) \quad \frac{d\bar{n}}{dz} = (\alpha - \eta)\bar{n}, \quad \frac{d\bar{p}}{dz} = \alpha\bar{n}$$

2558 which, assuming the initial conditions  
 2559  $\bar{n}(0) = 1$  and  $\bar{p}(0) = 0$ , leads to the mean  
 2560 number of electrons and cations at a depth  $z$

$$(3.11) \quad \begin{aligned} \bar{n}(z) &= e^{(\alpha-\eta)z} \\ \bar{p}(z) &= \frac{\alpha}{\alpha-\eta} \left( e^{(\alpha-\eta)z} - 1 \right) \end{aligned}$$

2561 The Townsend and attachment coefficient as a function of the applied electric field are given in  
 2562 Figure 3.31 for a standard RPC gas mixture using Magboltz [228].

2563 Nevertheless, there is more to the avalanche growth than simply these two factors. Throughout  
 2564 the 20<sup>th</sup> century, models have been developed to better understand the physics of discharges in gas.  
 2565 In 1937, Furry developed a model to describe electromagnetic cascades [227] that would be used for  
 2566 electron avalanches in gas during the 1950s. Furry realized that the use of a Poisson law to describe  
 2567 the distribution of shower sizes could not be accurate as he understood that the events occurring in  
 2568 the development of a cascade are not independent from each other, as a Poisson law would suggest.  
 2569 Indeed, part of the particles produce others and this process depends on both their original energy  
 2570 and energy lost. Compared to a Poissonian distribution, experimental results showed an excess of  
 2571 small showers and an underestimate of very large ones. To solve this problem, Furry proposed a  
 2572 distribution of sizes according to the likelihood described in Equation 3.12, in which  $\bar{n} = e^{\alpha z}$ . The  
 2573 Furry distribution is compared with a Poisson law in Figure 3.32.

$$(3.12) \quad P(n, \bar{n}) = \bar{n}^{-1} (1 - \bar{n}^{-1})^{n-1}$$

2574 In this model, no extra energy is brought to the electrons in the showers, contrary to the case  
 2575 of a gaseous detector such as an RPC where an electric field accelerates them. Using the Furry  
 2576 model, Genz studied the fluctuations in electron avalanches in gaseous detectors [229]. Collisions  
 2577 leading to ionizations leave electrons with an energy much smaller than the ionization energy  $eU_i$ ,  
 2578 where  $U_i$  is the ionization potential of a gas molecule. Hence, the electrons need to travel a distance  
 2579  $s = U_i/E$  along the electric field  $E$  to acquire a high enough energy to trigger a new ionization. For  
 2580 the probability of a new ionization to be independent from the path followed by the electrons since  
 2581 the previous ionization, the mean free path  $1/\alpha$  of electrons in the gas has to be large compared to  
 2582  $s$  and thus  $E/\alpha \gg U_i$ . The Townsend coefficient is related to the gas pressure  $p$ . Keeping  $E/\alpha$   
 2583 large compared to  $U_i$  implies that the value of  $E/p$  needs to stay lower than 100 V/cm/torr. In  
 2584 the case of proportional counters such as RPCs, avalanches are large compared to the showers Furry  
 2585 has studied in his original paper. For very large avalanche sizes, Equation 3.12 can be written as an  
 2586 exponential, as shown in Equation 3.13.

$$(3.13) \quad P(n, \bar{n}) = \bar{n}^{-1} e^{-n/\bar{n}}$$

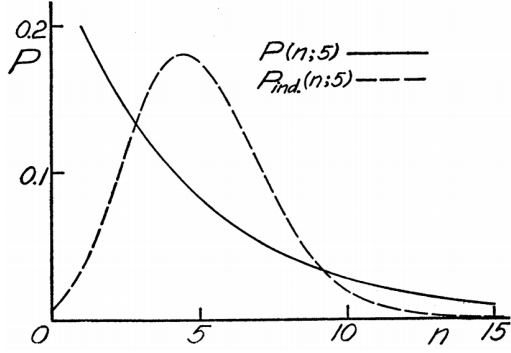


Figure 3.32: Comparison of the distribution law of Furry and the Poisson law for  $\bar{n} = 5$  [227].

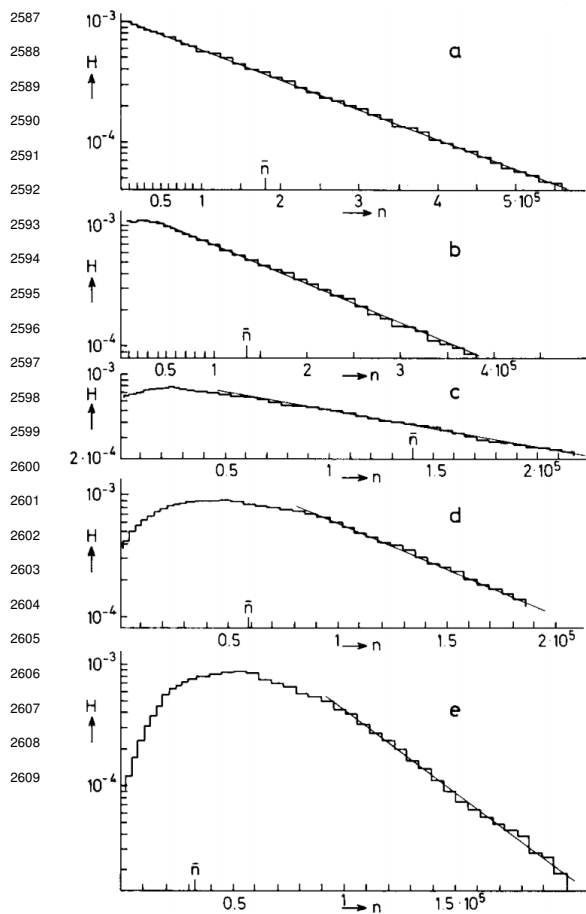


Figure 3.33: Single-electron avalanche size distribution in a proportional counter filled with methylal at different  $E/p$  values. (a) 70, (b) 76.5, (c) 105, (d) 186.5, (e) 426V/cm torr [229]. The straight lines correspond to an exponential fit.

ability better, the introduction of the attachment into the model is an important step. Despite its limitations, the Furry model had the advantage to well describe avalanches occurring when the attachment could be ignored. An extension of this model was provided by Riegler, Lippmann and Veenhof [222] who showed that it was important was to consider both the Townsend coefficient describing the multiplication *and* the attachment coefficient, and not only the effective multiplication coefficient  $\bar{\alpha} = \alpha - \eta$ . The probability to see an avalanche started by a single electron grow to a size  $n$  after having traveled a distance  $z$  through the gas is given by Equation 3.16.

$$\begin{aligned}
 P(n, z) &= P(n-1, z) (n-1)\alpha dz (1 - (n-1)\eta dz) \\
 (3.16) \quad &+ P(n, z) (1 - n\alpha dz) (1 - n\eta dz) \\
 &+ P(n, z) n\alpha dz n\eta dz \\
 &+ P(n+1, z) (1 - (n+1)\alpha dz) (n+1)\eta dz
 \end{aligned}$$

This exponential behaviour is illustrated in Figure 3.33. In practice, to fully understand the avalanche growth, taking into account the path followed by the electrons from one ionization to another is necessary. In the same paper, Genz then discusses models using Polya distributions to estimate the charge multiplication by looking at the size of the avalanche itself. Indeed, the number of charge carriers in the avalanche might become important enough to have an effect on the multiplication process. To account for this, it was proposed to use a varying Townsend coefficient such as described by Equation 3.14 depending on the depth  $x$  in the gas volume in which  $\theta$  is an empirical parameter leading to the probability distribution of Equation 3.15. In the limit where  $\theta$  goes to 0, the formula describes again the Furry model. But the data deviates from this model as well at large  $n$  values. Moreover, the introduction of an empirical parameter makes the model hard to interpret physically.

$$(3.14) \quad \alpha(n, x) = \alpha(x) \left( 1 + \frac{\theta}{n} \right), \quad n > 0$$

$$\begin{aligned}
 (3.15) \quad P(n, x) &= \frac{1 + \theta}{\bar{n}(x)} \frac{1}{\theta!} \left( \frac{n(1 + \theta)}{\bar{n}(x)} \right)^{\theta} e^{-\frac{n(1 + \theta)}{\bar{n}(x)}}
 \end{aligned}$$

In order to have a model that describes re-

The first term of this probability describes that from a state with  $n - 1$  electrons, only 1 multiplies while the others don't get attached. Both the second and third terms describes the probability that from a state with already  $n$  electrons the total number of electrons stay the same. With the second term, no electron gets attached nor multiplies while with the third term, 1 electron gets multiplied and 1 gets attached to compensate. Finally, the fourth term describes the probability to fall from a state with  $n + 1$  to a state with  $n$  electrons due to the attachment of a single electron. At the first order, the evaluation of the previous expression leads to Equation 3.17 whose general solution is given in Equation 3.18. The variables  $\bar{n}(z)$ , defined as in Equation 3.11, and  $k = \eta/\alpha$  making explicit the fact that the distribution does not depend on the effective Townsend coefficient only are introduced in the equation.

$$(3.17) \quad \frac{dP(n, z)}{dz} = -P(n, z)n(\alpha + \eta) + P(n - 1, z)(n - 1)\alpha + P(n + 1, z)(n + 1)\eta$$

$$(3.18) \quad P(n, z) = \begin{cases} k \frac{\bar{n}(z)-1}{\bar{n}(z)-k}, & n = 0 \\ \bar{n}(z) \left( \frac{1-k}{\bar{n}(z)-k} \right)^2 \left( \frac{\bar{n}(z)-1}{\bar{n}(z)-k} \right)^{n-1}, & n > 0 \end{cases}$$

The example given in Figure 3.34 shows the importance of each individual process in the growth of avalanches and the fluctuation of their size. The values of  $\alpha$  and  $\eta$  will influence the probability distribution, as can be seen from Figure 3.34a. Then, Figure 3.34b shows that the fluctuation really takes place within the very first interactions. Indeed, when the avalanche contains a large enough number of charge carriers (a few hundred), its size increases like  $e^{z(\alpha-\eta)}$ .

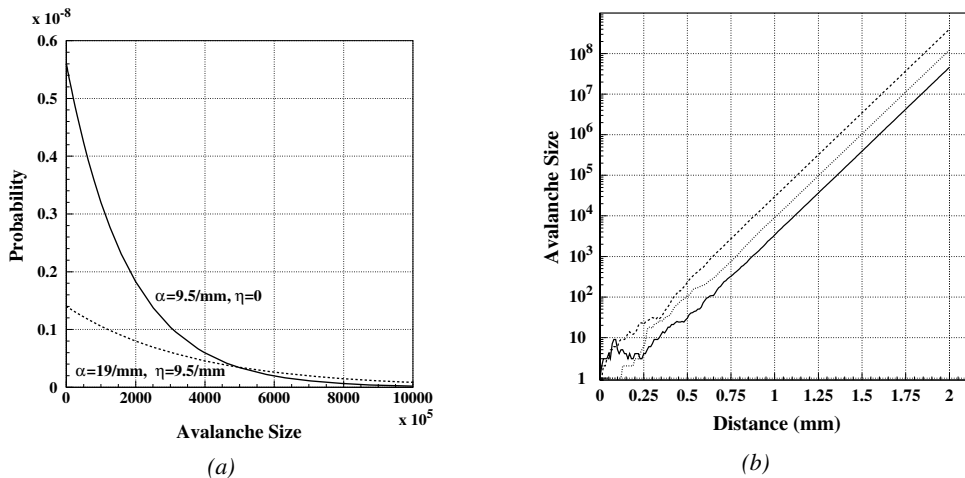


Figure 3.34: (a): Comparison of avalanche size distributions for different values of Townsend and attachment coefficients. The effective Townsend coefficient is the same for both distributions. (b): Fluctuation in avalanche sizes for avalanches started by a single electron with  $\alpha = 13 \text{ mm}^{-1}$  and  $\eta = 3.5 \text{ mm}^{-1}$  [222].

### 3.3.4 Drift and diffusion of the electron cloud

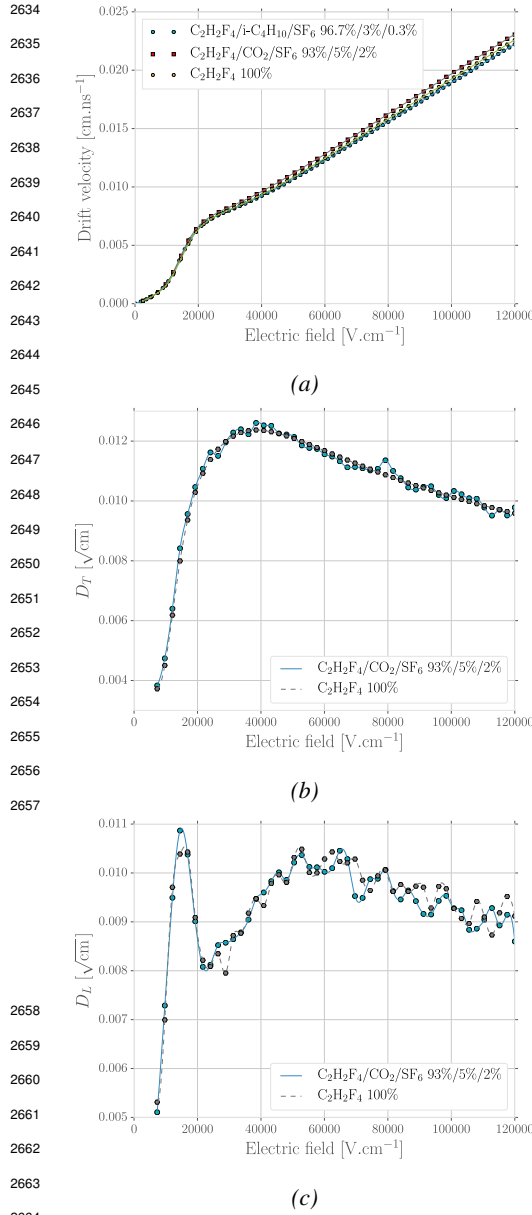


Figure 3.35: (a): Electrons mean drift velocity  $v_D$  in pure  $C_2H_2F_4$  and typical RPC gas mixtures. (b): Transverse diffusion coefficient in pure  $C_2H_2F_4$  and a typical RPC gas mixture. (c): Longitudinal diffusion coefficient in pure  $C_2H_2F_4$  and a typical RPC gas mixture. All results are given for a pressure  $P = 760$  Torr and a temperature  $T = 296.15$  K [215].

$$(3.20) \quad \varphi_T(r, t) = \frac{1}{D_T^2 l} \exp\left(-\frac{(r - r_0)^2}{2D_T^2 l}\right)$$

During the growth of avalanches, an electron cloud drifting along the electric field through the gas will undergo thermal diffusion due to random collisions with the gas molecules. This phenomenon can be studied using the Maxwell-Boltzmann distribution whose mean is defined by the thermal energy of the cloud  $\langle E \rangle = 3/2kT$  with an extra component coming from the constant drift motion. The drift of electrons along the field lines is usually observed on a macroscopic scale through which the speed can be assimilated to a constant  $v_D$  which corresponds to the mean drift speed over a large number of collisions in the gas.

At the microscopic scale, the electrons are drifting over a distance  $\delta z$  while acquiring the corresponding kinetic energy  $T = e_0 |\vec{E}| \delta z$  until they are slowed down by a collision in which they lose part of their energy. This process is repeated as long as electrons are free carriers. Starting at time  $t = 0$  from a point-like electron cloud at a position  $\vec{r}_0$ , the Gaussian density distribution at a time  $t$  will be described by Equation 3.19 in which the width of the isotropic distribution is  $\sigma = 2\bar{D}t$ , with  $\bar{D}$  being a diffusion coefficient expressed in m<sup>2</sup>/s [197].

$$(3.19) \quad \varphi(\vec{r}, t) = \frac{1}{(\sqrt{2\pi}\sigma(t))^3} \exp\left(-\frac{(\vec{r} - \vec{r}_0)^2}{2\sigma^2(t)}\right)$$

Now, if the constant drifting motion is added, the distribution is anisotropic and can be divided onto transversal (Equation 3.20) and longitudinal (Equation 3.21) terms,  $\varphi(r, z, t) = \varphi_T(r, t)\varphi_L(z, t)$ , with a cylindrical symmetry around the field axis [197]. The dependence on  $t$  and  $\sigma_{T,L}(t)$  can be absorbed into the diffusion coefficients by using the relations  $v_D = l/t$  and  $\sigma_{T,L}^2(t) = 2\bar{D}_{T,L}l/v_D$  and introducing new diffusion coefficients  $D_{T,L} = \sqrt{2\bar{D}_{T,L}/v_D}$  in order to explicitly show the dependence of the Gaussian width in drifted distance  $l$ .

$$(3.21) \quad \varphi_L(z, t) = \frac{1}{\sqrt{2\pi l D_L}} \exp\left(-\frac{(z - z_0)^2}{2D_L^2 l}\right)$$

These coefficients, as well as the drift velocity of the electrons, can be calculated thanks to Magboltz as shown in Figure 3.35. The influence of the diffusion on the distribution of charge carriers throughout the gas volume is depicted in Figure 3.36. From very localised electron clusters in the gas in Figure 3.36a, a Gaussian diffusion is then visible in Figure 3.36b. Due to the interactions with gas molecules during the drift, diffusions can occur in the forward and backward direction. Electrons diffused backward will effectively drift over a longer distance and multiply more than electrons diffused forward that will see a shorter drift length. As an effect, the avalanche develops over a longer time and extends over a larger gas volume than in the case the electron cloud is considered as point like and without diffusion. Moreover, as a side effect to the longer growth of the avalanche due to backward longitudinal diffusion, the total production of electrons is increased.

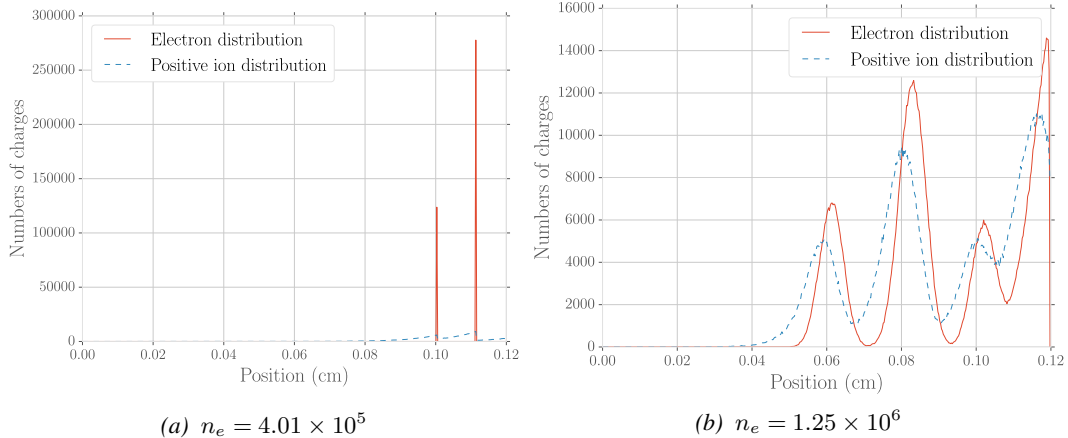


Figure 3.36: Comparison of the free charge carriers in the gas after a time  $t = 7.90$  ns in the case where no diffusion is taken into account to simulate the avalanche (a) and in the case where the diffusion is implemented (b) [215].

### 3.3.5 Space charge effect & streamers

In addition to the basic processes that influence the development of avalanches in a gaseous detector, it is important to consider also the influence of the charge carriers present in the avalanche on the electric field seen by the avalanche. Indeed, each charged particle induces an electric field and it is only natural that the increasing density of electrons and ions in the detector volume will affect the electric field. Thus, parameters such as the Townsend and attachment coefficients, drift velocity or diffusion coefficients will find themselves to be modified along the gas gap length due to this effect referred to as *space charge effect*. Figure 3.37 is a more detailed version of Figure 3.1b in which three electric field regions are distinguished [197]. When compared to the linear electric field of strength  $E_0$  that is developed in between the detector's electrodes, the accumulation of negative charges (electrons) on the front of the avalanche will reinforce the effective electric field in between the anode and the avalanche front. Deeper in the gas volume, the positive charges (cations) slowly drift towards the cathode and can induce together with the avalanche front opposite electric field

loops. Finally, due to the density of positive charges, the electric field seen in between the ions tails and the cathode charged with negative charges is on average stronger than  $E_0$  and compensate for the locally reversed field  $E_2$ . By considering that  $10^6$  charges were contained in a sphere of radius  $r_d = 0.1$  mm Lippmann roughly estimated that the space charge effect could change the electric field by 3% and the Townsend and attachment coefficient up to 14% [197, 215].

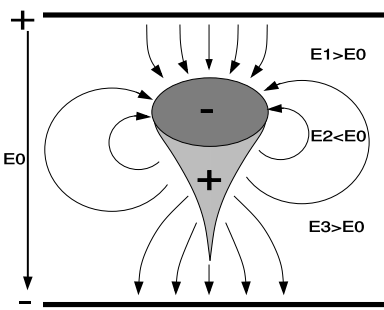


Figure 3.37: Schematic representation of an avalanche and of the electric field deformation it causes due to the local concentration of charge carriers [197].

To account for the space charge effect, the electric potential and field of free charges are solved and applied to each charge in the avalanche [197, 215]. The computation of these equations for each individual charge carrier to dynamically know the space charge field at every stage of an avalanche development is a difficult task and would require far too much computation time. A solution is to pre-compute an interpolation table keeping an adequately large number of values of the space charge field for each position in space. The values stored in the interpolation table then become very close to the analytic solution and allow for a much faster simulation.

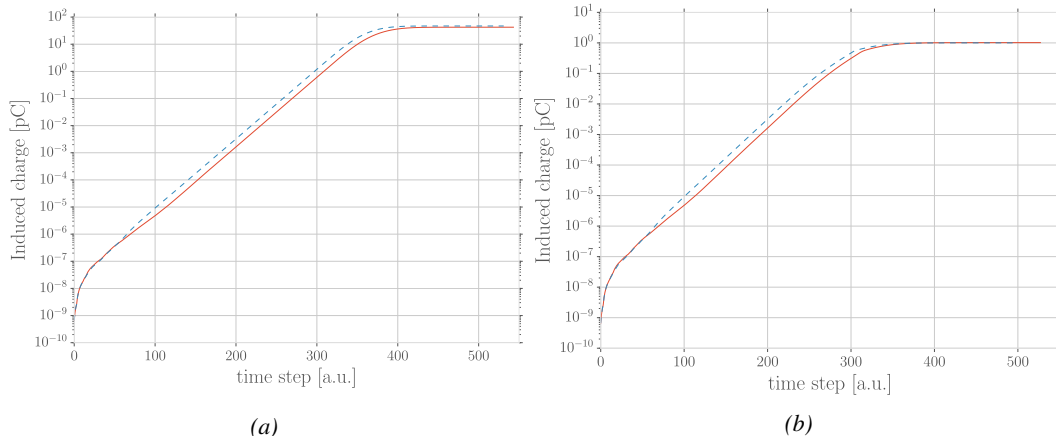


Figure 3.38: Evolution of the charge induced by an avalanche started by a single electron in a 1.2 mm thick RPC with an applied electric field of 54 kV/cm in the case space charge is not taken into account (a) and in the case it is implemented into the simulation (b). The total induced charge is correlated to the size of the avalanche [215].

The study of the space charge effect through simulation shows that it can lead to a saturation of the avalanche growth due to the deformation of the electric field, as showed through Figure 3.38. Additionally, a more precise understanding of the space charge effect is given through Figure 3.39 which looks at the distribution of charges and the distortion of the electric field at different steps of the evolution of an avalanche in a RPC. At the moment a 5 GeV muon ionizes the gas, electron-ion pairs are created in the gas in different clusters (Figure 3.39a). Later, the first clusters have reached the anode while the clusters that were created closest to the cathode are now big enough to start influencing the electric field in the gap (Figure 3.39b). When a cluster is big enough, the electric field

in front of it locally increases a lot and contributes to a stronger but very localised multiplication. At the same moment, the positive ions right behind the cluster avalanche front decrease the electric field, saturating the electron multiplication on the tail of the electron cloud (Figure 3.39c). Finally, when all the electrons have reached the anode and are recombining, the electric field still is very deformed by the distribution of both positive and negative ions in the gas volume closest to the anode (Figure 3.39d).

The electric field following the development of an avalanche can stay perturbed for a long time with respect to the avalanche development due to the slow drift of the much heavier ions. This can result in powerful secondary avalanches triggered by the fluctuation of the electric field together with the emission of UV-photons. This is a slow phenomenon compared to the development of avalanches. Experimentally, it is observed that the stronger the electric field applied over the gap, the sooner after the primary avalanche, referred to as *precursor signal* in this context, and the stronger the secondary avalanche will be. This could be due to the amount of UV-photons emitted by the growing precursor. These photons will be able to trigger new avalanches in a radius of a few mm around the precursor by knocking electrons from the cathode by photoelectric effect. The strong distortions of the electric field due to a large avalanche will be more likely to emit UV-photons as the electric field at the front of the precursor avalanche will be large, providing the electrons with a larger energy. Eventually, the new avalanches can grow to form streamers.

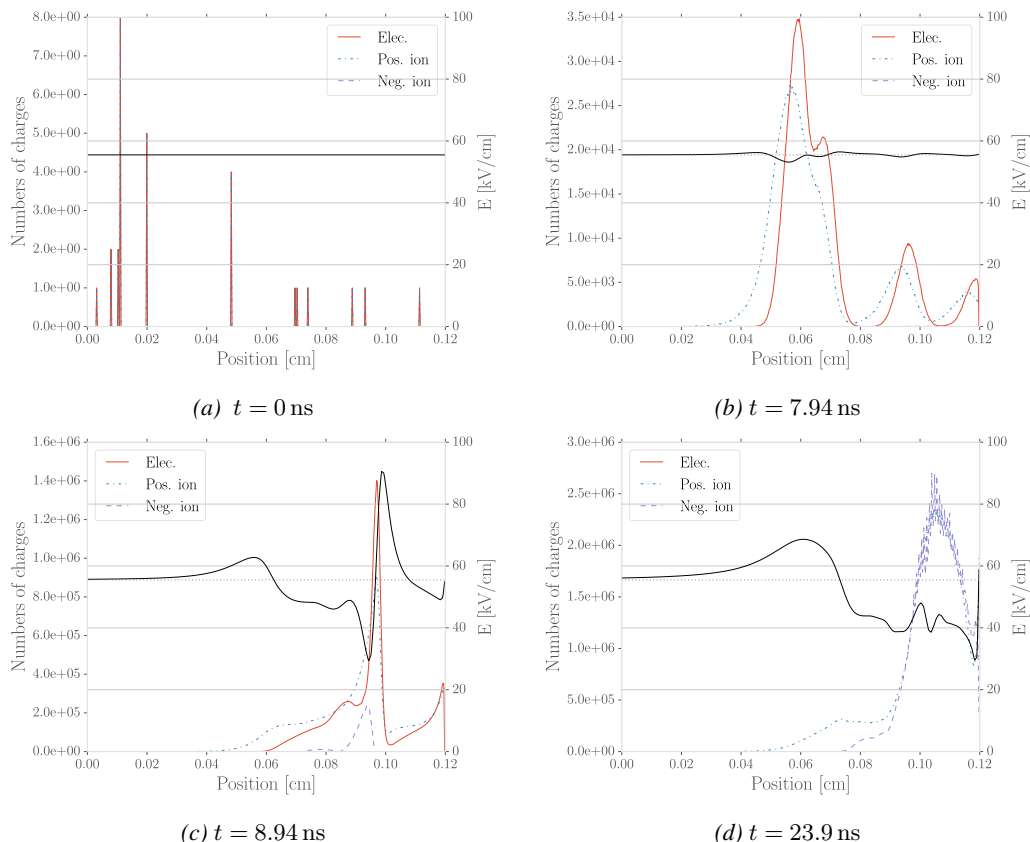


Figure 3.39: Distributions of charge carriers within the gas volume of a 1.2 mm thick RPC and the corresponding deformation of the electric field at different time steps with an applied electric field of 55.5 kV/cm [215].

### 3.4 Effect of atmospherical conditions

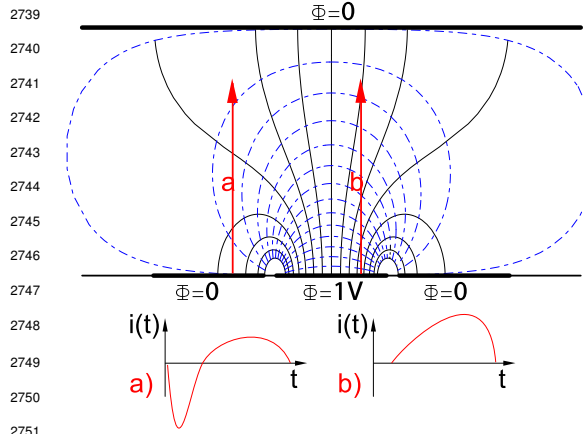


Figure 3.40: Representation of the weighting field in the volume of an RPC and the resulting induced current in the strip placed at 1 V and its neighbour connected to the ground. The induced current corresponds, as can be understood from Formula 3.22 [197].

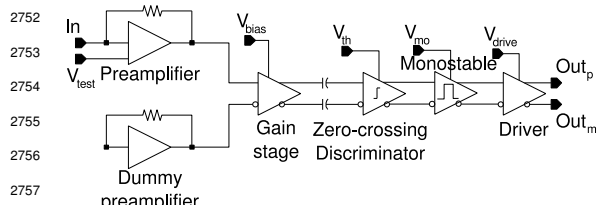


Figure 3.41: Schematics of CMS RPC FEE logic.

Formula 3.23.

$$(3.23) \quad Q(t) = \int_0^T \sum_{j=1}^{n_{Cl}} \vec{E}_{wj}(\vec{x}_j(t)) \cdot \vec{v}_{Dj}(t) e_0 N_j(t)$$

The signal induced in the readout of RPCs operated in avalanche mode is then sent into Front-End Electronics in which they will be pre-amplified and discriminated. The discrimination and digitization of signals in CMS FEE are described through Figure 3.41. On a first stage, analog signals are amplified, following the curve given on Figure 3.42, and then sent to a Constant Fraction Discriminator (CFD). At the end of the chain, 100 ns long pulses are sent to the LVDS output. The digital signals are both used as trigger for CMS and to evaluate the performance of the detectors. The performance will depend on the applied HV, i.e. on the electric field inside of the gas volume, but also on the threshold applied on the CFDs. Indeed, in order to reduce the probability to measure noise, the threshold is set to a level where the noise is strongly suppressed while the signals are not too affected. Typically, CMS FEEs are set to a threshold of 215 mV after pre-amplification, corresponding to an input charge of about 140 fC.

Accordingly to the Shockley-Ramo theorem, the movement of charge carriers, and in particular, the movement of a dense electron cloud toward the anode induces a current signal on one or more of the readout electrodes (strips or pads) [230, 231]. The ions, on the other hand, induce only a very small current as their movement is much slower than which of the electrons. The current induced by  $n_{Cl}$  clusters of  $N_j(t)$  charge carriers drifting at velocities  $\vec{v}_{Dj}(t) = \vec{x}_j(t)$  at a time  $t$  is given by Formula 3.22 in which  $e_0$  is the unit charge and  $\vec{E}_w$  is the weighting field.

(3.22)

$$i(t) = \sum_{j=1}^{n_{Cl}} \vec{E}_{wj}(\vec{x}_j(t)) \cdot \vec{v}_{Dj}(t) e_0 N_j(t)$$

The weighting field, depicted in Figure 3.40, corresponds to the electric field that would be observed in the gas gap if a readout electrode is placed at a potential of 1 V while keeping all the other electrodes grounded. Then the induced charge in the readout can be simply obtained by integrating Formula 3.22 over the duration  $T$  of the signal, as given by

The efficiency of a detector can be measured using a reference detector used as trigger as the ratio between the number of events recorded in coincidence in the detector and the reference and the total number of trigger events,  $\epsilon = n_{events}/n_{triggers}$ . An example of an efficiency measurement as a function of the effective voltage  $HV_{eff}$  is given in Figure 3.43. The data can be fitted with a sigmoidal function described as in Equation 3.24, where  $\epsilon_{max}$  is the maximal efficiency of the detector,  $\lambda$  is proportional to the slope at half maximum and  $HV_{50}$  is the value of the voltage when the efficiency reaches half of the maximum.

$$(3.24) \quad \epsilon(HV_{eff}) = \frac{\epsilon_{max}}{1 + e^{-\lambda(HV_{eff} - HV_{50})}}$$

CMS RPC also define two points on this sigmoid that called *knee* and *working point*.  $HV_{knee}$  is defined as the voltage at 95% of the maximum efficiency, and  $HV_{WP}$  is defined as in Formula 3.25.

$$(3.25) \quad HV_{WP} = HV_{knee} + \begin{cases} 100V & \text{barrel} \\ 150V & \text{endcap} \\ 120V & \text{before LS1} \\ & \text{endcap} \\ & \text{after LS1} \end{cases}$$

Nevertheless, the voltage applied on a detector may vary due to a change in environmental conditions. Indeed, the variation of temperature and/or pressure will have effect on the gas density and the electrode resistivity. This can be compensated by changing the electric field accordingly. The influence of variation in temperature and pressure are depicted respectively in Figure 3.44 and Figure 3.45. A standard procedure to correct for temperature and pressure variations is to keep the factor  $HV \cdot T/P$  constant using Formula 3.26 [232, 233] with reference values for  $T_0$  and  $P_0$ . For example, CMS uses  $T_0 = 293.15$  K and  $P_0 = 965$  hPa.

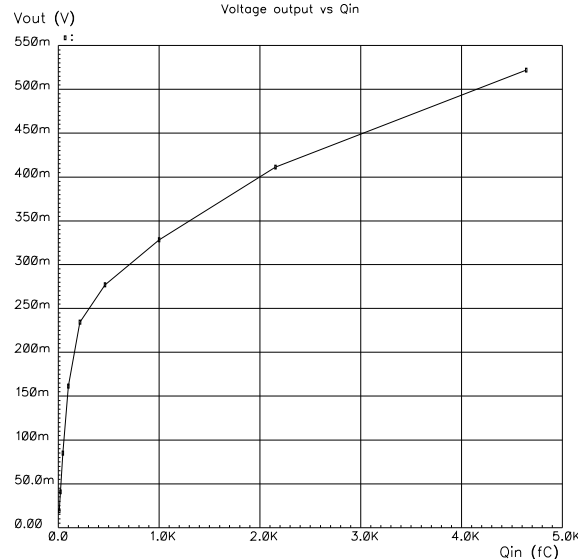


Figure 3.42: Equivalence in between the charge of the induced signal in input of the CMS FEE and the signal strength on the output of the pre-amplifier.

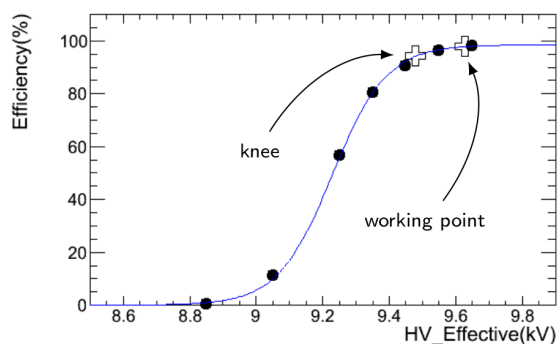
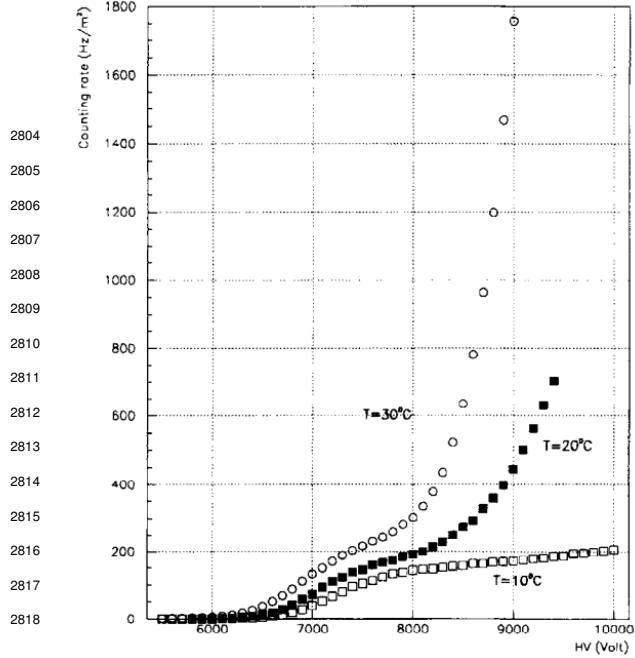
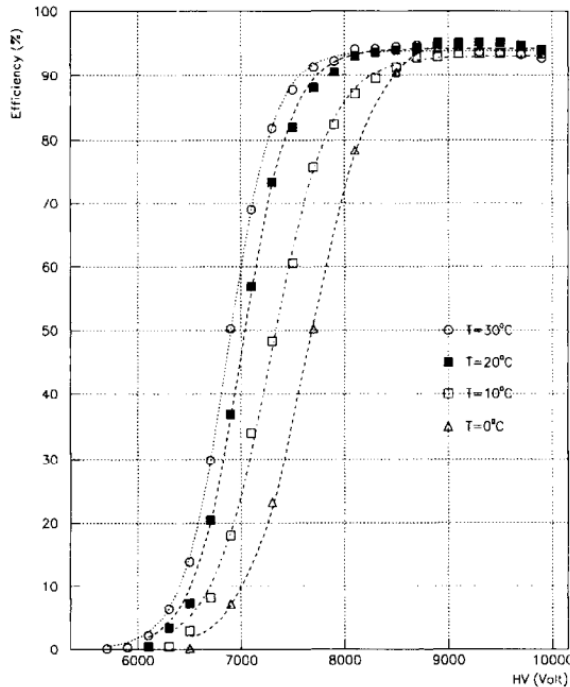


Figure 3.43: Typical efficiency sigmoid of a CMS RPC detector. The black dots correspond to the data, the blue line to the sigmoid fit and the open cross to the knee and working point extracted from the fit.



(a)



(b)

Figure 3.44: Effect of the temperature variation on the rate (a) and the efficiency (b) of an RPC [232].

$$(3.26) \quad HV_{app} = HV_{eff} \frac{P_0}{P} \frac{T}{T_0}$$

It was actually found that such a simple procedure overcorrects the applied voltage in case the variations of temperature or pressure become significant [234–237]. CMS, considering that the temperature variations in the detector cavern were very small, decided only to improve the pressure correction, giving rise to Formula 3.27 [234] while on the other hand, ATLAS decided to have a more robust correction for both parameters and uses Formula 3.28 instead [237]. The coefficients  $\alpha$ , in the case of CMS, and  $\alpha, \beta$ , in the case of ATLAS, are extracted from a fit to data obtained during the operation of the detectors.

$$(3.27) \quad HV_{app} = HV_{eff} \left( 1 - \alpha + \alpha \frac{P_0}{P} \right) \frac{T}{T_0}$$

$$\alpha = 0.8$$

$$(3.28) \quad HV_{eff} = HV_{app} \left( 1 + \alpha \frac{\Delta T}{T_0} \right) \left( 1 - \beta \frac{\Delta P}{P_0} \right)$$

$$\alpha = 0.5, \beta = 0.71$$

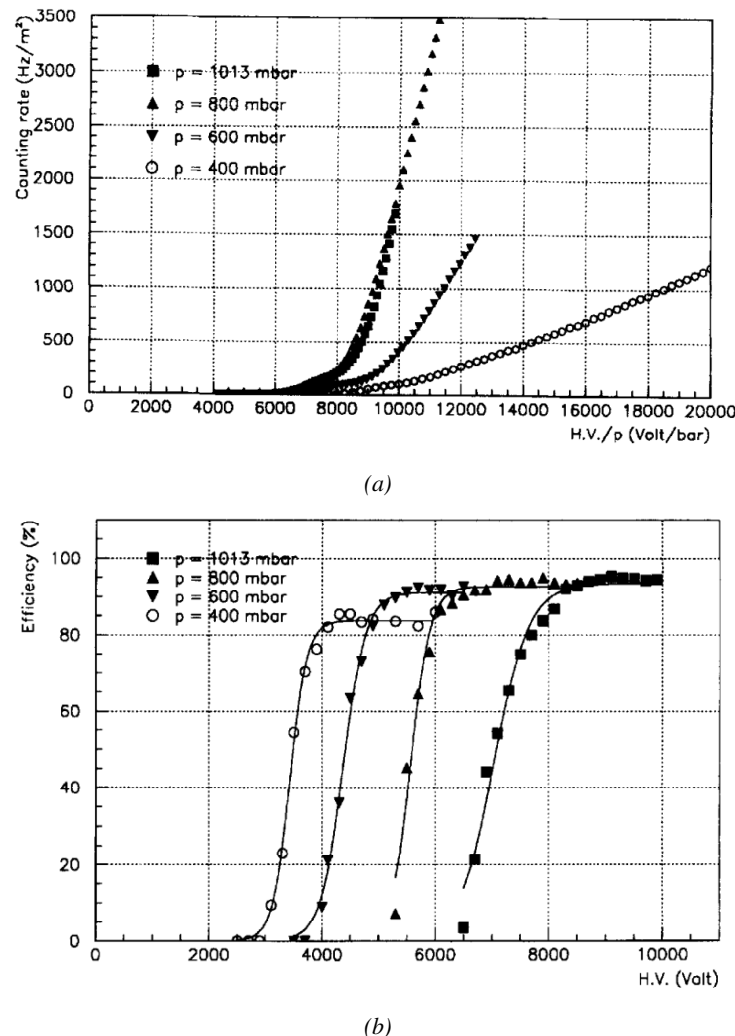


Figure 3.45: Effect of the pressure variation on the rate (a) and the efficiency (b) of an RPC [233].

